
THE UNIVERSITY OF ARIZONA
University Libraries

UA CAMPUS
REPOSITORY

Efficient Methanol Production on the Dark Side of a Prestellar Core

Item Type	Article
Authors	Harju, Jorma; Pineda, Jaime E.; Vasyunin, Anton I.; Caselli, Paola; Offner, Stella S. R.; Goodman, Alyssa A.; Juvela, Mika; Sipilä, Olli; Faure, Alexandre; Le Gal, Romane; Hily-Blant, Pierre; Alves, João; Bizzocchi, Luca; Burkert, Andreas; Chen, Hope; Friesen, Rachel K.; Güsten, Rolf; Myers, Philip C.; Punanova, Anna; Rist, Claire; Rosolowsky, Erik; Schlemmer, Stephan; Shirley, Yancy; Spezzano, Silvia; Vastel, Charlotte; Wiesenfeld, Laurent
Citation	Jorma Harju et al 2020 ApJ 895 101
DOI	10.3847/1538-4357/ab8f93
Publisher	IOP PUBLISHING LTD
Journal	ASTROPHYSICAL JOURNAL
Rights	Copyright © 2020. The American Astronomical Society. All rights reserved.
Download date	19/07/2021 10:58:38
Item License	http://iopscience.iop.org/info/page/text-and-data-mining
Version	Final published version
Link to Item	http://hdl.handle.net/10150/641898

The Astrophysical Journal, 895:101 (18pp), 2020 June 1 https://doi.org/10.3847/1538-4357/ab8f93
© 2020. The American Astronomical Society. All rights reserved.

Efficient Methanol Production on the Dark Side of a Prestellar Core

Jorma Harju[1,2], Jaime E. Pineda[1], Anton I. Vasyunin[1,3,4], Paola Caselli[1], Stella S. R. Offner[5], Alyssa A. Goodman[6], Mika Juvela[2], Olli Sipilä[1], Alexandre Faure[7,8], Romane Le Gal[6], Pierre Hily-Blant[7,8], João Alves[9], Luca Bizzocchi[1], Andreas Burkert[1,10], Hope Chen[6], Rachel K. Friesen[11], Rolf Güsten[12], Philip C. Myers[6], Anna Punanova[1,3], Claire Rist[7,8], Erik Rosolowsky[13], Stephan Schlemmer[14], Yancy Shirley[15], Silvia Spezzano[1], Charlotte Vastel[16,17], and Laurent Wiesenfeld[18]

[1] Max-Planck-Institut für extraterrestrische Physik, Gießenbachstraße 1, D-85748 Garching, Germany
[2] Department of Physics, P.O. BOX 64, FI-00014 University of Helsinki, Finland
[3] Ural Federal University, 620002, 19 Mira street, Yekaterinburg, Russia
[4] Ventspils University of Applied Sciences, Inženieru 101, Ventspils 3601, Latvia
[5] Astronomy Department, University of Texas, Austin, TX 78712, USA
[6] Harvard-Smithsonian Center for Astrophysics, 60 Garden Street, Cambridge MA 02138, USA
[7] Université Grenoble Alpes, IPAG, F-38000 Grenoble, France
[8] CNRS, IPAG, F-38000 Grenoble, France
[9] University of Vienna, Türkenschanzstraße 17, A-1880 Vienna, Austria
[10] Universitäts-Sternwarte, Ludwig-Maximilians-Universität München, Scheinerstraße 1, D-81679 München, Germany
[11] Dunlap Institute for Astronomy and Astrophysics, University of Toronto, 50 St. George Street, Toronto M5S 3H4, Ontario, Canada
[12] Max-Planck-Institut für Radioastronomie, Auf dem Hügel 69, D-53121 Bonn, Germany
[13] Department of Physics, 4-181 CCIS, University of Alberta, Edmonton, AB T6G 2E1, Canada
[14] I. Physikalisches Institut, Universität zu Köln, Zülpicher Straße 77, D-50937 Köln, Germany
[15] Steward Observatory, University of Arizona, 933 North Cherry Avenue, Tucson, AZ 85721, USA
[16] Université de Toulouse, UPS-OMP, IRAP, Toulouse, France
[17] CNRS, IRAP, 9 Avenue du Colonel Roche, BP 44346, F-31028 Toulouse Cedex 4, France
[18] Laboratoire Aimé-Cotton, CNRS and Université Paris-Saclay, F-91405 Orsay, France
Received 2020 March 17; revised 2020 April 29; accepted 2020 April 30; published 2020 June 2

Abstract

We present Atacama Large Millimeter/submillimeter Array maps of the starless molecular cloud core Ophiuchus/H-MM1 in the lines of deuterated ammonia (ortho-NH_2D), methanol (CH_3OH), and sulfur monoxide (SO). The dense core is seen in NH_2D emission, whereas the CH_3OH and SO distributions form a halo surrounding the core. Because methanol is formed on grain surfaces, its emission highlights regions where desorption from grains is particularly efficient. Methanol and sulfur monoxide are most abundant in a narrow zone that follows the eastern side of the core. This side is sheltered from the stronger external radiation field coming from the west. We show that photodissociation on the illuminated side can give rise to an asymmetric methanol distribution but that the stark contrast observed in H-MM1 is hard to explain without assuming enhanced desorption on the shaded side. The region of the brightest emission has a wavy structure that rolls up at one end. This is the signature of Kelvin–Helmholtz instability occurring in sheared flows. We suggest that in this zone, methanol and sulfur are released as a result of grain–grain collisions induced by shear vorticity.

Unified Astronomy Thesaurus concepts: Interstellar molecules (849); Astrochemistry (75); Interstellar dust processes (838); Dense interstellar clouds (371)

1. Introduction

Gaseous methanol (CH_3OH) has been found to be present in the outer parts of cold starless cores, with abundances of the order of 10^{-9} relative to H_2 (Bizzocchi et al. 2014; Vastel et al. 2014; Jiménez-Serra et al. 2016; Spezzano et al. 2016; Punanova et al. 2018). The derived abundances exceed the predictions from pure gas-phase chemical models by orders of magnitude (Garrod et al. 2006; Bacmann & Faure 2016). Methanol is believed to form almost exclusively on the surfaces of dust grains via hydrogenation of frozen carbon monoxide (CO; Watanabe & Kouchi 2002; Geppert et al. 2006), and it is a common constituent of interstellar ices. To be detectable in the gas phase, methanol must be released from grains as a result of heating or some nonthermal mechanism. In cold, starless cores, nonthermal processes, such as impulsive heating by cosmic-ray collisions (Leger et al. 1985; Hasegawa & Herbst 1993; Roberts et al. 2007; Kalvāns 2018a) and desorption caused by exothermic surface reactions (Garrod et al. 2006, 2007; Vasyunin & Herbst 2013; Balucani et al. 2015; Jiménez-Serra et al. 2016; Vasyunin et al. 2017), provide plausible explanations for the observed fractional abundances and distributions of methanol.

It should be noted, however, that core boundaries, where methanol is usually found, are also subject to dynamical effects, such as accretion, velocity shears, and turbulence. Several cores show a sharp transition from supersonic to subsonic turbulence in a thin layer surrounding the core (Goodman et al. 1998; Pineda et al. 2010; Friesen et al. 2017; Auddy et al. 2019). In this region, the scaling relation between the velocity dispersion, σ_v, and the scale length l, $\sigma_v \propto l^a$, seems to break (Goodman et al. 1998), suggesting that part of the turbulent energy of the surrounding gas is dissipated, while at the same time, the exterior turbulence compresses the core. Also, gravitational accretion from the surrounding cloud and collisions between cores can lead to conversion of kinetic energy into heat. These effects can contribute to the evaporation of the ice coatings of dust grains.

Table 1
Spectral Lines Observed toward Ophiuchus/H-MM1 with ALMA

Molecule	Transition	Frequency (MHz)	E_u (K)	A_{ul} (10^{-5} s^{-1})	Δv (m s^{-1})	rms[a] (K)
o-NH_2D	$1_{11} - 1_{01}$	85926.27	20.7	0.78	107	0.042
CH_3OH	$2_{-1} - 1_{-1}$ E	96739.36	12.5	0.26	95	0.049
	$2_0 - 1_0$ A	96741.38	7.0	0.34		
	$2_0 - 1_0$ E	96744.55	20.1	0.34		
	$2_1 - 1_1$ E	96755.51	26.9	0.26		
SO	$2_3 - 1_2$	99299.87	9.2	1.13	1474	0.011

Note.
[a] Beam size 4″.

Photodesorption and photodissociation caused by the external radiation field can affect the chemical composition in the outer parts of the dense cores (Hollenbach et al. 2009). The effect is particularly strong in the vicinity of young massive stars (e.g., Gaches & Offner 2018), and when the core lies near the edge of a cloud (Spezzano et al. 2016). Radiation is also the main source of heat at the core boundaries. Finally, cosmic-rays, which both heat and ionize gas, may also drive chemical changes (e.g., Caselli et al. 2012; Maret et al. 2013; Cleeves et al. 2016). While the cosmic-ray flux is often assumed to be uniform throughout star-forming regions, cosmic-rays can be accelerated locally by protostellar jets and accretion shocks, causing the cosmic-ray flux to vary spatially on core and cloud scales (Padovani et al. 2016). This, in turn, produces chemical gradients in dense gas (Cleeves et al. 2014; Gaches et al. 2019).

Here, we present maps of a nearby prestellar core in the spectral lines of methanol, deuterated ammonia (NH_2D), and sulfur monoxide (SO), obtained using the Atacama Large (Sub) millimeter Array (ALMA). We discuss the origin of gas-phase methanol based on the observed molecular distributions and the physical conditions of the emission regions. In addition to cosmic-ray collisions and reactive desorption, we identify grain–grain collisions induced by gas velocity fluctuations as a possible mechanism releasing methanol from grains. In this connection, we consider grain acceleration in three-dimensional turbulence and in shear vorticity. The influence of the external radiation field on the asymmetries of the CH_3OH and SO distributions is also discussed.

2. Observations

The target of the present observations is the nearby prestellar core Ophiuchus/H-MM1 located on the eastern side of the L1688 cloud (Johnstone et al. 2004; Parise et al. 2011; Harju et al. 2017). The dimensions of the kidney-shaped dense core are approximately $1' \times 2'$. The target is prominent in the 850 μm dust continuum maps of Ophiuchus observed with SCUBA-2 (Pattle et al. 2015) and in the NH_3 map of L1688 from the Green Bank Ammonia Survey (GAS; Friesen et al. 2017).

The present data were taken during ALMA cycle 4 (project 2016.1.00035.S). Here, we discuss the $J_k = 2_k - 1_k$ rotational lines of CH_3OH at 96.7 GHz and the $J_{K_a,K_c} = 1^s_{11} - 1^a_{01}$ rotation-inversion line of ortho-NH_2D at 85.9 GHz, which were observed simultaneously with the 3 millimeter continuum in ALMA Band 3. The "continuum" spectral window included the $J_N = 3_2 - 2_1$ rotation line of SO at 99.3 GHz. This line is unresolved because the channel width in this spectral cube is ∼4.9 MHz (∼1.5 km s^{-1}, see Table 1).

An area of $95'' \times 135''$ covering the brightest 850 μm emission was imaged using the ALMA 12 m array (40 antennas) in one of its most compact configurations, and the ALMA Compact Array (ACA) with ten 7 m antennas. The total power antennas were not used. With the 12 m array, the mapping was carried out by a five-point mosaic, whereas with the 7 m array, a single point was measured. The data were calibrated and imaged using the CASA version 4.7.2. The synthesized beam sizes of naturally weighted images ranged from $3\farcs8 \times 2\farcs5$ (at 85.9 GHz) to $3\farcs5 \times 2\farcs3$ (at 99.3 GHz). The largest recoverable scale of the images is approximately 60″. In what follows, we use image cubes that were created using a common, circular 4″ restoring beam for all lines. Based on recent distance determinations for L1688 using the Very Long Baseline Array and Gaia (Ortiz-León et al. 2017; Ortiz-León et al. 2018), we adopt a distance of 140 pc for the core. The angular resolution 4″ corresponds to 560 au at this distance. The observed transitions are listed in Table 1. The rms noise values in Table 1 are given for the image cubes with 4″ resolution. For the 3 mm continuum map, the rms noise is approximately 0.06 mJy beam^{-1}.

3. Integrated Intensity Maps

The integrated intensity maps of the ortho-NH_2D, CH_3OH, and SO lines at 85.9, 96.7, and 99.3 GHz, respectively, are shown in Figures 1(a), (b), and (c). The methanol map is also shown in panel (c) as contours superposed on the SO map. The fourth map, shown in panel (d) of this figure, is the H_2 column density map derived from 8 μm extinction. For this, we have used the 8 μm surface brightness map measured by the InfraRed Array Camera (IRAC) of the Spitzer Space Telescope, smoothed to a 4″ resolution (the original resolution is ∼2″). The method used for deriving the $N(H_2)$ map is described in Appendix A. The 3 mm continuum emission is weak with a peak intensity of ∼0.3 mJy beam^{-1}, that is, five times the rms noise of the map. The continuum sensitivity of the present ALMA observations was not sufficient for detecting extended emission around this peak. The 3 mm continuum map using only the ACA data is shown in Figure 1(d), as a contour plot superposed on the $N(H_2)$ image.

The NH_2D map resembles the H_2 column density map shown in Figure 1(d) and the far-infrared dust emission maps of the core, e.g., the 850 μm SCUBA-2 map shown in Figure B1. The CH_3OH and SO distributions closely resemble each other (see Figure 1(c)), and they are almost complementary to the NH_2D distribution; methanol and sulfur monoxide follow the edges of the elongated core but are stronger on the left, concave side of the core (the eastern side in the sky) than elsewhere.

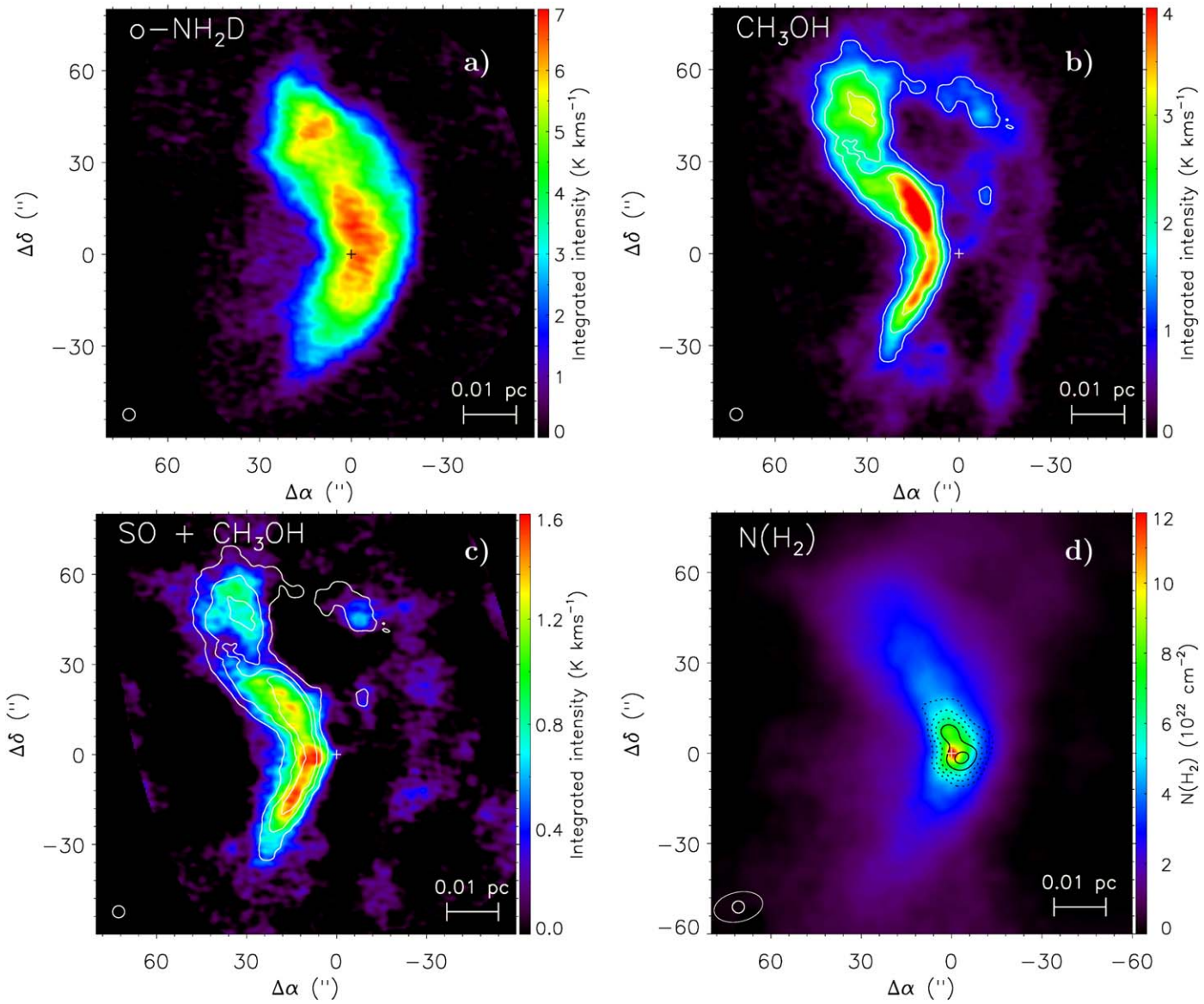

Figure 1. Molecular line maps and the H_2 column density map of the Ophiuchus/H-MM1 core. Panels (a), (b), and (c) show the integrated intensity maps of the ortho-$NH_2D(1_{11}–1_{01})$, $CH_3OH(2_k - 1_k)$, and $SO(2_3 - 1_2)$ lines measured by ALMA. Methanol contours are superposed on the SO map in panel (c). The contour levels are 1, 2, and 3 K km s^{-1}. The synthetic beam size of the ALMA images (4″) is indicated in the bottom left of each panel. The $N(H_2)$ map of panel (d) is derived from 8 μm extinction, based on observations by the Spitzer Space Telescope. The contour lines show the 3 mm continuum emission measured by the ACA. The levels go from 2 to 3 mJy beam^{-1} in steps of 0.25 mJy beam^{-1}. The ellipse in the bottom left represents the synthetic beam of the ACA map. The plus sign indicates the position of the column density maximum with the coordinates R.A. 16:27:58.65, decl. −24:33:41.2 (J2000).

4. Column Densities and Velocity Distributions

Four lines of the $(2_k - 1_k)$ group of CH_3OH were included in the spectral window around 96.7 GHz. Three of them belong to the E symmetry species and one to the A species. The rotational temperatures, T_{rot}, and the column densities, N, of E-type methanol were derived adopting the procedure described by Nummelin et al. (2000), where no assumption about the optical thickness of the lines is made. The calculation was limited to the positions where at least two of the $E - CH_3OH$ lines are detected with 3σ significance. In practice, this means positions where the integrated intensity of the $2_0 - 1_0$ line is greater than $\sim$0.045 K km s^{-1}. The region where this condition holds is contained within the 1 K km s^{-1} contour of the total integrated intensity map shown in Figures 1(b) and (c). The weighted average of the rotational temperature and its standard deviation are $\bar{T}_{rot} = 10.3 \pm 0.7$ K. The peak value of the E-methanol column density is $N(E - CH_3OH) = 1.1 \pm 0.1 \times 10^{14}$ cm^{-2}. In the region with the brightest CH_3OH emission, bordering the eastern side of the core, $N(E - CH_3OH) \geqslant 5 \times 10^{13}$ cm^{-2}. On the western side, the column density could only be determined toward irregularly dispersed positions. The values in these positions are typically less than $\sim 5 \times 10^{12}$ cm^{-2}, except for a couple of positions reaching $\sim 2 \times 10^{13}$ cm^{-2}. The A-methanol column density, $N(A - CH_3OH)$, was estimated using the single A-line in the spectrum, assuming that the rotational temperatures of the A and E symmetry species are the same. The weighted average of the A/E ratio and its standard deviation is 1.3 ± 0.2 (the high-temperature statistical value is 1.0). This indicates that $N(CH_3OH) \sim 2 \times N(E - CH_3OH)$.

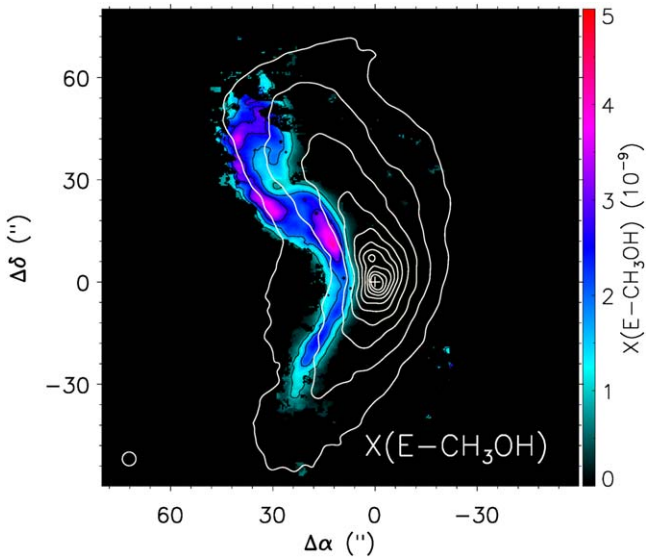

Figure 2. Fractional $E-CH_3OH$ abundance distribution. The contours represent the H_2 column density. They go from 1×10^{22} to 10×10^{22} cm^{-2} in steps of 1×10^{22} cm^{-2}.

The data set contains only one spectrally unresolved SO line, $J_N = 3_2 - 2_1$, at 99.3 GHz. Therefore, we only can derive the lower limit of the SO column density assuming optically thin emission. In this approximation, the upper state column density is directly proportional to the integrated brightness temperature, $\int T_B\, dv$, of the line. A rotation temperature, assumed to be the same for all rotational transitions, needs to be adopted for the calculation of the partition function. Assuming $T_{rot} = 10$ K, we get $N(SO) = 1.2 \times 10^{13}\,\mathrm{cm^{-2}} \times \int T_B\, dv$, when the integral is in K km s^{-1}. For $T_{rot} = 5$ K, the numerical factor before the integral is 1.7×10^{13} cm^{-2}.

The fractional CH_3OH and SO abundance distributions were determined by dividing the column density maps by the $N(H_2)$ map shown in Figure 1(d). The fractional CH_3OH abundance map is shown in Figure 2. The highest methanol abundances, $X(CH_3OH) \sim 8 \times 10^{-9}$ (assuming equal abundances for the E and A types) are found at the eastern border of the core. The SO abundances are highest south of the methanol peak, with $X(SO) \sim (0.7\text{–}1.0) \times 10^{-9}$, depending on the assumed T_{rot} (10 or 5 K).

In this paper, we only use the kinematic information from the NH_2D lines; the NH_2D column densities and fractional abundances will be discussed elsewhere. The ortho-NH_2D spectral cube was analyzed by performing multicomponent Gaussian fits to the hyperfine structure of the 1_{11}–1_{01} line, which consists of five separate groups of hyperfine components, four satellites located symmetrically on both sides of the strongest main group. The model used for the hyperfine structure takes into account the splittings owing to the electric quadrupole moments of both N and D nuclei (Daniel et al. 2016). The fits were made to positions where each of the outer satellites are detected with 3σ significance, meaning that their integrated intensity is greater than $\sim$0.050 K km s^{-1}. These fits give accurate estimates for the line velocity and width. The velocity distribution of methanol was derived by Gaussian fits to the four lines near 96.7 GHz. In this fitting, the line separations were fixed, and it was assumed that the velocity dispersion is the same for all components.

Multicomponent Gaussian fits to the NH_2D and CH_3OH lines were used to produce collapsed line profiles, that is, single Gaussians with the same integrated intensity, radial velocity, and velocity dispersion as the original lines consisting of several frequency components. Radial velocity channel maps over the velocity range 3.9–4.4 km s^{-1} derived from the collapsed NH_2D and CH_3OH profiles are shown in Figure 3 (the full range of detectable emission is 3.7–4.6 km s^{-1}). The velocity dispersion maps are shown in Figure 4. A similar analysis was not possible for the unresolved SO spectra.

The channel maps of Figure 3 show an overall north–south gradient. The velocity change (including all channels with detectable emission) is approximately 0.7 km s^{-1} over a distance of 0.034 pc, corresponding to 50″ in the sky. The core motion is reminiscent of an eddy rather than rigid body rotation and seems to support the idea of core formation in turbulent converging flows (Gong & Ostriker 2011). Despite an east–west offset, CH_3OH and NH_2D follow the same velocity pattern, and it is remarkable how the NH_2D peak in each channel is found some 10″–20″ west of the CH_3OH peak. Methanol lines, originating at the core boundaries, have larger line-of-sight velocity dispersions than NH_2D lines (Figure 4). Histograms of the one-dimensional velocity dispersions of the lines are shown in Figure 5. This figure indicates that the line widths of NH_2D are nearly thermal, assuming a kinetic temperature of 10 K, whereas CH_3OH lines have a substantial nonthermal component. However, also for CH_3OH, the velocity dispersion is subsonic in most positions.

The relationship between the CH_3OH and NH_2D distributions in space and velocity is visualized in a video available at https://www.youtube.com/watch?v=C814sOPF7c0. This video demonstrates the superimposition of the CH_3OH and NH_2D data cubes using Glue[19], which is an open-source Python library designed for the analysis of multidimensional related data sets. The close complementarity of the two distributions is particularly evident in this video.

5. Note on the NH_2D Distribution

Ammonia and its deuterated isotopologues form both in the gas and on grains, and they are subject to accretion and desorption just like CH_3OH and SO. Why is the distribution of NH_2D, then, so different from those of CH_3OH and SO? One thing that affects this difference is that ammonia (along with some other nitrogen containing molecules; Hily-Blant et al. 2010) is less susceptible to freeze-out than most C- and O-bearing molecules. This observational fact is not fully understood (Sipilä et al. 2019). The persistence of gaseous ammonia is evident, for example, from the GAS maps of nearby molecular clouds (Friesen et al. 2017; see also the maps in Tafalla et al. 2006). Harju et al. (2017) suggested that one of the reasons for this persistence is the chemical inertia of N_2 molecules on grain surfaces, which makes them return to the gas phase rather than form chemical bonds on the surface.

The other reason for the contrasting distributions of NH_2D and CH_3OH is that deuterium fractionation starts in earnest at high densities where CO has largely disappeared from the gas, whereas CH_3OH production (through desorption) is probably most active further out in a starless core, where CO is not severely depleted (see Section 6). In the gas phase, deuterated ammonia is mainly produced in reactions between NH_3 and

[19] https://glueviz.org

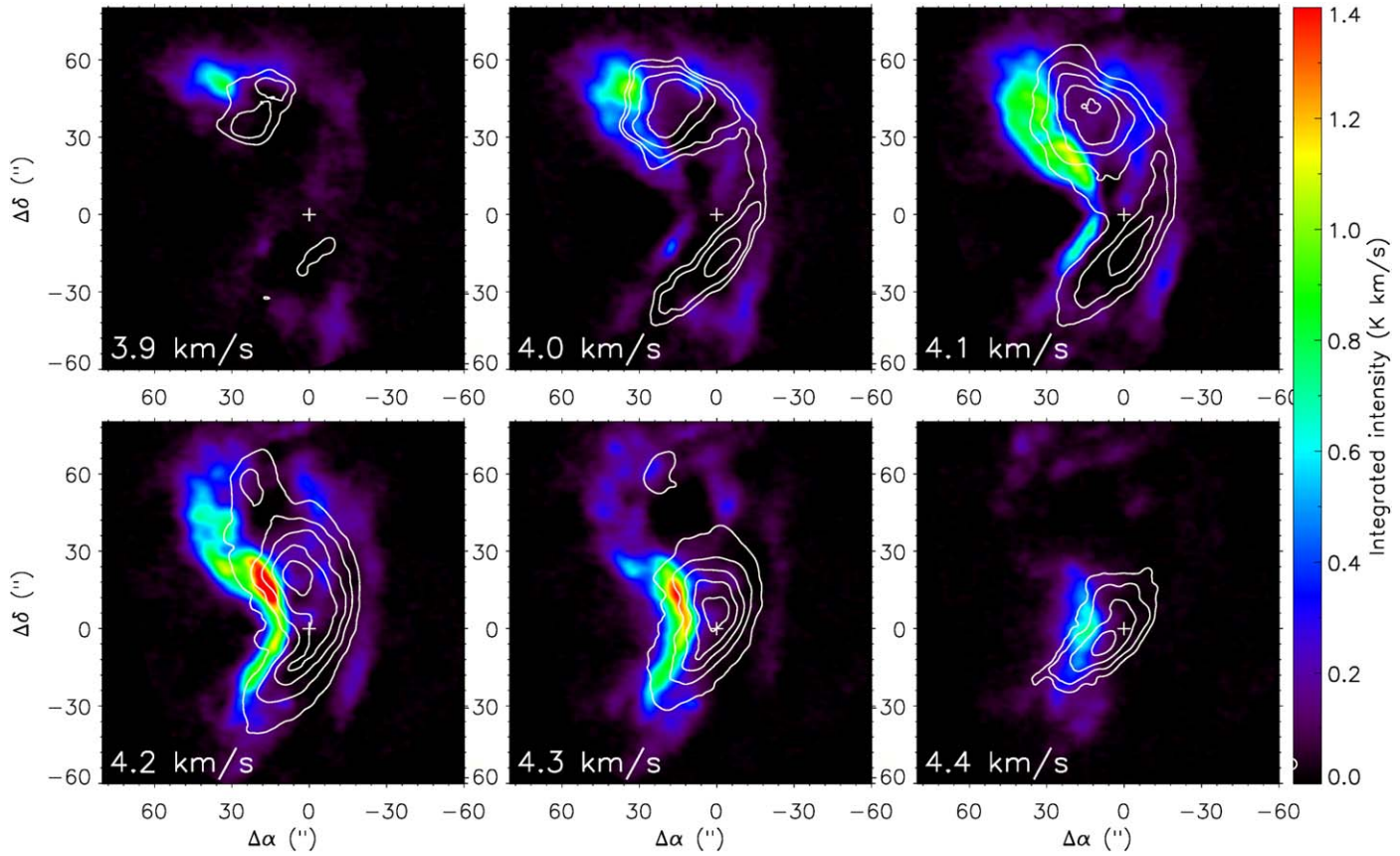

Figure 3. Velocity channel maps of CH_3OH and NH_2D (contours) emissions. The contour levels of the NH_2D maps are: 0.2 and 0.4 K km s^{-1} (3.9 km s^{-1}); 0.2, 0.4, 0.8, and 1.4 K km s^{-1} (4.0 and 4.4 km s^{-1}); and 0.2, 0.4, 0.8, 1.4, 2.0, and 2.6 K km s^{-1} (4.1–4.3 km s^{-1}).

deuterated ions (Rodgers & Charnley 2001; Sipilä et al. 2015; Hily-Blant et al. 2018). Deuterated ions are enhanced as a consequence of the freeze-out of CO, which first leads to a rapid increase of H_3^+. Deuterium fractionation is boosted when the fractional CO abundance decreases below that of HD, $\sim 3 \times 10^{-5}$. The primary fractionation reaction is $H_3^+ + HD \rightarrow H_2D^+ + H_2$. Successive reactions with HD also produce D_2H^+ and D_3^+. In cold, dense clouds, the deuterated forms of H_3^+ compete for the position of dominant ion and transfer deuterium to other species including NH_3 (Roberts et al. 2003; Walmsley et al. 2004; Caselli et al. 2019).

Ammonia attains high abundances on grains, where it is formed through H atom additions to N atoms. The formation of NH_2D and other deuterated molecules on grains thus requires free D atoms, which usually have very low abundances in molecular clouds, as almost all deuterium is locked in HD. The abundance of free D atoms increases, however, significantly when deuterium chemistry flourishes in the gas phase. The principal source of deuterium atoms is the dissociative electron recombinations of the H_2D^+, D_2H^+, and D_3^+ ions, which benefit from the depletion of CO. The production of NH_2D is therefore strongly favored inside the CO depletion zone. The predicted radial distributions of the fractional abundances for different ammonia isotopologues in a dense starless core model resembling H-MM1 are shown in Figure 14 of Harju et al. (2017). Because the H_2 density distribution is centrally peaked, the NH_2D column density is also highest at the core center. In H-MM1, the detectable NH_2D emission is confined to the dense region that can be seen as a dark patch on the 8 and 24 μm surface brightness maps (see Appendices A and B).

6. Desorption of Methanol

In this section, we describe mechanisms that can release methanol from grains and estimate their efficiencies in a cold, dense cloud. This is to provide background for the next Section, where we discuss the origin of the asymmetric methanol distribution observed in H-MM1 with ALMA.

The binding energy of methanol on a water ice surface is approximately 5500 K (0.47 eV), and its thermal evaporation from interstellar grains is likely to become significant at around 100 K, where H_2O and NH_3 also sublimate (Garrod & Herbst 2006). In the interiors of dense starless clouds, the otherwise cold dust grains can be impulsively heated by various mechanisms, leading to the desorption of methanol and other species formed on their surfaces. Moreover, UV photons created in cosmic-ray collisions with H_2 molecules can contribute to the desorption of the mantle material. Also, a combination of different mechanisms may be effective. For example, impulsive heating by a cosmic-ray can trigger a chain of radical–radical reactions and an explosive release of chemical energy stored in the grain mantle (d'Hendecourt et al. 1982; Leger et al. 1985; Ivlev et al. 2015b). In the experiments of d'Hendecourt et al. (1982), explosive events in grain mantle analogs always occurred at $\sim$27 K, probably because radicals in their samples became mobile at this temperature. However, no runaway reaction was observed without preceding UV photolysis, which was needed to produce the radicals. The number of incident photons in their experiment was 20% of the number of sample molecules, and

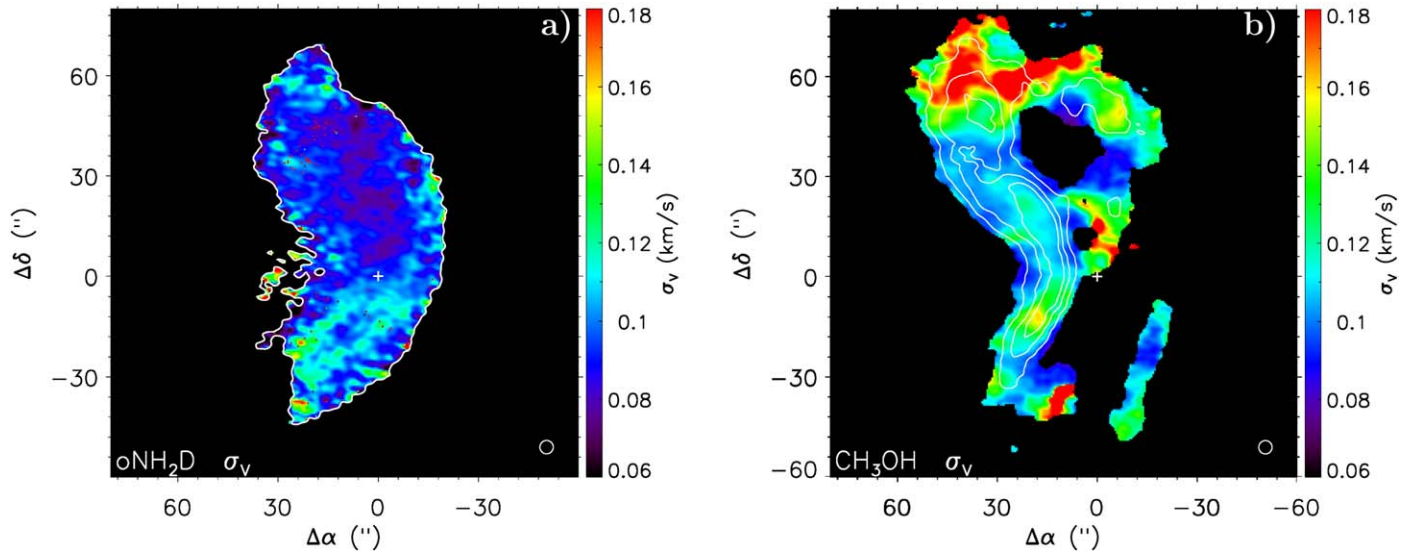

Figure 4. Velocity dispersions of NH_2D, panel (a), and CH_3OH, panel (b), spectral lines.

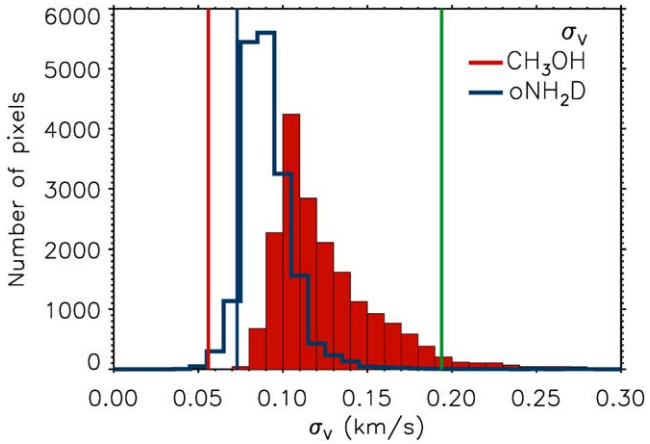

Figure 5. One-dimensional velocity dispersions of the ortho-NH_2D and CH_3OH lines. The blue and red vertical lines indicate the thermal velocity dispersions of NH_2D and CH_3OH at 10 K. The green vertical line indicates the sound speed at this temperature.

they estimate that a ratio of 10% could still be sufficient for explosive ejection.

A grain constantly accretes atoms and molecules from the gas, including CO and the highly mobile H atoms, and this alone could be thought to result in the accumulation of radicals in the icy mantle. The number of radicals formed through accretion is likely to be small, however, compared to that of saturated molecules because of efficient hydrogenation and oxidation of surface species. The characteristic fraction of reactive molecules has been estimated to be maximally a few percent (Leger et al. 1985; Ivlev et al. 2015b). Models and observations suggest that the grain mantle has a layered structure with water ice in the bottom, covered by layers of CO ice that forms at higher densities (Tielens & Hagen 1982; Whittet et al. 2001; Pontoppidan 2006). According to the model results of Cuppen et al. (2009), the mantle surfaces are dominated by CH_3OH ice in cold dense cores, while CO and other less-saturated species remain locked in the lower ice layers. The complete hydrogenation of CO to CH_3OH is favored in conditions where CO freezes out ($n(H_2) \gtrsim 10^5\,\mathrm{cm}^{-3}$, $T \lesssim 15$ K), depending on the H/CO abundance ratio in the gas phase (Cuppen et al. 2009).

6.1. Cosmic-Ray-induced Desorption

Cosmic-ray-induced desorption is supposed to sustain traceable gas-phase abundances of O- and C-bearing molecules also in the inner parts of cold, dense clouds (e.g., Leger et al. 1985; Hasegawa & Herbst 1993; Shen et al. 2004; Roberts et al. 2007; Hollenbach et al. 2009). The efficiency of cosmic-ray-induced sputtering of methanol embedded in water ice has been studied experimentally by Dartois et al. (2019). In their Figure 11, Dartois et al. (2019) present estimates for CH_3OH sputtering rates as functions of the cosmic-ray ionization rate for two methanol fractions in the ice, 0.55 and 0.056, with respect to H_2O. The lower of these fractions is characteristic of interstellar ices (Boogert et al. 2015). Assuming that the cosmic-ray ionization rate of H_2 is $\zeta^{H_2} \sim 6 \times 10^{-17}\,\mathrm{s}^{-1}$ at the core boundary, one obtains from Figure 11 of Dartois et al. (2019) that the flux of sputtered CH_3OH molecules is $F^{sp}_{CH_3OH} \sim 0.14\,\mathrm{cm}^{-2}\,\mathrm{s}^{-1}$ (here, we have multiplied the value indicated in the figure by two to account for the exiting cosmic-ray, as suggested in the caption). The adopted ζ^{H_2} is consistent with the models of Padovani et al. (2009), in view of the fact that the H_2 column density of the ambient cloud around H-MM1 is $\sim 10^{22}\,\mathrm{cm}^{-2}$.

In order to estimate the desorption rate per H atom or per cubic centimeter in the interstellar medium, we adopt the MRN grain size distribution (Mathis et al. 1977). This is a power-law distribution of spherical grains with $\frac{dn_g}{da} \propto a^{-3.5}$ between $a_{min} = 0.005\,\mu$m (50 Å) and $a_{max} = 0.25\,\mu$m, where a is the grain radius, and n_g is the number density of grains. Assuming that the dust-to-gas mass ratio is 0.01 and that the average grain material density is 3.0 g cm^{-3}, the cross-sectional area of dust grains is $\sigma_H = 1.64 \times 10^{-21}\,\mathrm{cm}^2$ per H atom. The cosmic-ray-induced sputtering rate of CH_3OH from water ice is then $\sim 2.3 \times 10^{-22}$ molecules s^{-1} per H atom. The rate per cubic centimeter and second can be obtained by multiplying this number by the total hydrogen density n_H, which is $\sim 2 \times n(H_2)$ in molecular clouds. The corresponding desorption rate per methanol molecule is $\sim 5.7 \times 10^{-17}\,\mathrm{mol}^{-1}\,\mathrm{s}^{-1}$, assuming that

the fractional methanol abundance on grains relative to H atoms is $n(CH_3OH, s)/n_H \sim 4 \times 10^{-6}$. This abundance is derived using the composition of the ice mantles in quiescent clouds and cores listed in Table 2 of Boogert et al. (2015), assuming that the mantle constitutes 15% of the grain mass. The adopted CH_3OH abundance agrees reasonably well with gas-grain chemistry models (e.g., Taquet et al. 2014; Vasyunin et al. 2017). Dartois et al. (2019) estimate that the flux of sputtered CH_3OH from CO ice is 40 times higher than that from water ice, which gives a methanol sputtering rate of $\sim 9 \times 10^{-21}$ s^{-1} per H atom or $\sim 2 \times 10^{-15}$ mol^{-1} s^{-1}.

By way of comparison, the direct cosmic-ray-induced desorption rate of water in conditions described above can be estimated to be $\sim 4.6 \times 10^{-21}$ s^{-1} per H atom or $\sim 9.3 \times 10^{-17}$ mol^{-1} s^{-1}. Here, we have used the sputtering flux from water ice derived by Faure et al. (2019), $F^{sp}_{H_2O} \sim f_{H_2O}\ 0.8\ \zeta^{H_2}/10^{-17}$ cm^{-2} s^{-1}, where $f_{H_2O} \sim 0.6$ is the fraction of water molecules in the ice according to Table 2 of Boogert et al. (2015; see also Equation (7) of Faure et al. 2019). The fractional water abundance relative to H atoms, $n(H_2O, s)/n_H \sim 5 \times 10^{-5}$, is estimated in the same manner as the fractional methanol abundance above. Because of similar binding energies of H_2O and CH_3OH, the desorption rate estimate of Faure et al. (2019) should also be adequate for methanol when corrected for the methanol fraction, ~0.08 with respect to H_2O. The resulting CH_3OH desorption rate ($\sim 3.7 \times 10^{-22}$ s^{-1} per H atom or $\sim 9.3 \times 10^{-17}$ mol^{-1} s^{-1}) is ~60% higher than that derived using data from Dartois et al. (2019). On the other hand, applying similar scaling to the cosmic-ray-induced sputtering rate per water molecule, 4.4×10^{-17} mol^{-1} s^{-1}, derived by Bringa & Johnson (2004), brings us very close to the result of Dartois et al. (2019), with a methanol sputtering rate of $\sim 1.8 \times 10^{-22}$ s^{-1} per H atom or 4.4×10^{-17} mol^{-1} s^{-1}. Finally, we note that the cosmic-ray desorption rate per methanol molecule used by Hasegawa & Herbst (1993) is very low compared to the values quoted above, 6.3×10^{-20} mol^{-1} s^{-1} ($\sim 2.5 \times 10^{-25}$ s^{-1} per H atom).

6.2. Cosmic Ray-induced Photodesorption and Dissociation

Photodissociation and photodesorption by the external far-ultraviolet (FUV) radiation field are considered to be important near cloud boundaries up to an efficient visual extinction of $A_V \sim 5^{mag}$ (Hollenbach et al. 2009; Keto et al. 2014). Stellar radiation in the Ophiuchus complex is exceptionally strong. Hollenbach et al. (2009) assume that the FUV radiation field in the vicinity of the core Oph A in the western part of the complex is 300 times the average local interstellar radiation field in that band as that determined by Habing (1968; often denoted by G_0). Assuming that the FUV field is attenuated by 20 magnitudes in the ambient cloud (corresponding to an effective visual extinction of $A_V \sim 10^{mag}$; e.g., Cardelli et al. 1989), the FUV flux at the core boundaries is $\sim 3 \times 10^{-6}\ G_0$, that is, ~300 FUV photons cm^{-2} s^{-1}. We model the FUV field and its attenuation in the case of H-MM1 in Section 7.1 below.

Cosmic-ray protons and secondary electrons from cosmic-ray ionization sustain a flux of Lyman and Werner band photons (11.2–13.6 eV) through the collisional excitation of H_2 to excited electronic states (Cecchi-Pestellini & Aiello 1992). According to the estimates of Cecchi-Pestellini & Aiello (1992) and Kalvāns (2018b), the flux of cosmic-ray-induced FUV photons is ~3000–5000 cm^{-2} s^{-1} in the interiors of dense dark clouds. Often, a flux value of 10^4 cm^{-2} s^{-1} or $10^{-4}\ G_0$ is used in chemistry models (e.g., Keto et al. 2014).

The experimental results of Bertin et al. (2016) and Cruz-Diaz et al. (2016) indicate that the efficiency of FUV photodesorption of methanol is low, of the order of 10^{-5} molecules per incident photon. Assuming that dust grains are fully covered by methanol ice, the photodesorption rate corresponding to this efficiency is $\sim 3.3 \times 10^{-22}$ methanol molecules s^{-1} per H atom. Using the composition of the ice mantles in quiescent clouds and cores listed in Table 2 of Boogert et al. (2015), with ~5% methanol, the photodesorption rate becomes $\sim 1.6 \times 10^{-23}$ s^{-1} per H atom (4.1×10^{-18} mol^{-1} s^{-1}). Here, we have adopted the FUV flux 5000 cm^{-2} s^{-1} from Cecchi-Pestellini & Aiello (1992) and used the total surface area of grains ($4 \times \sigma_H$) from the MRN size distribution.

Öberg et al. (2009) measured an average loss rate of condensed methanol of $\sim 10^{-3}$/photon in irradiated ices. This loss rate is probably attributable to photodissociation, producing fragments such as CH_3, OH, and CH_3O, that can remain in the ice mantle or be ejected into the gas phase (Bertin et al. 2016; Cruz-Diaz et al. 2016). The FUV photodissociation cross section of methanol ice is $\sim 2.7 \times 10^{-18}$ cm^2 (Öberg et al. 2009; Cruz-Diaz et al. 2016), so the photodissociation rate per methanol molecule caused by the cosmic-ray-induced FUV flux 5000 cm^{-2} s^{-1} is $\sim 1.3 \times 10^{-14}$ mol^{-1} s^{-1} (corresponding to $\sim 5.4 \times 10^{-20}$ s^{-1} per H atom, assuming $X(CH_3OH, s) = 4 \times 10^{-6}$).

Is cosmic-ray-induced photodissociation of mantle species an important source of chemical energy in dark cores? The ice mantle is supposed to constitute 15%–30% of the grain mass in dense dark clouds, and it is mainly composed of H_2O, CO, CO_2, CH_3OH, NH_3, and CH_4 (Boogert et al. 2015). Assuming that the mantle mass is 15% of that of the silicate core, one can calculate, adopting the same FUV flux as above, that the number of photons impinging onto a grain surface reaches 10% of the number of mantle molecules in ~8000 yr. The 10% ratio of the number incident FUV photons to the number of molecules was considered crucial in the experiment of d'Hendecourt et al. (1982). The answer to the question asked above depends on the average number of heatings to the critical temperature 27 K during the quoted period of time.

Whole grain heating by cosmic-rays has been recently modeled by Kalvāns (2018a) and Kalvāns & Kalnin (2019). Using estimates of the energy spectrum of cosmic-rays and their fluxes in molecular clouds from Padovani et al. (2009) and Chabot (2016), Kalvāns has derived cosmic-ray heating rates that (for moderate extinctions) are clearly higher than earlier estimates (see Figure 9 in Kalvāns 2018a). According to this work, grains residing in an obscured cold cloud ($A_V \sim 10^{mag}$) are heated to 27 K every ~900 yr (Kalvāns 2018a; their Table 19). This interval is an order of magnitude shorter than the time needed for the accumulation of any substantial amount of radicals through cosmic-ray-induced photolysis.

6.3. Reactive Desorption

In reactive desorption, a molecule forming on a grain escapes into the gas phase with the help of the exothermicity of the formation reaction, without any external agent such as a cosmic-ray or a photon (e.g., Garrod et al. 2006, 2007; Dulieu et al. 2013; Vasyunin & Herbst 2013; Minissale et al. 2016). The exothermicities of CO hydrogenation reactions are of the

order of a few eV, exceeding thus clearly the binding energies of the products. The question is: which part of the released energy goes to the breaking of the chemical bond to the surface and how much goes to the heating of the grain (Garrod et al. 2006)?

One can derive an estimate for the production rate of gaseous methanol assuming that a certain fraction, f_{CO}, of CO molecules hitting grains will be completely hydrogenated to methanol and that a fraction, f_{CH_3OH}, of methanol molecules so formed will be ejected into the gas. Garrod et al. (2006) found that a low value of the hydrogenation factor, $f_{CO} \sim 0.003$, reproduces the observed methanol abundances in their model. Another, much higher value of $f_{CO} \sim 0.13$ can be derived based on the relative abundances of carbon-bearing ice molecules in dark clouds ices listed in Boogert et al. (2015).

The fraction of desorbed products, f_{CH_3OH}, also called the efficiency of reactive desorption, has been found to depend strongly on the substrate, so that it is much larger for a rigid surface than for amorphous water ice (Minissale et al. 2016 and references therein). Based on the theoretical description of the reactive desorption efficiency presented by Minissale et al. (2016), Vasyunin et al. (2017) assumed that the efficiency of methanol desorption upon formation on a CO-rich surface is of the order of 1%. Similar desorption efficiencies have been used in previous works (for example, Garrod et al. 2007 and Vasyunin & Herbst 2013). According to the model of Vasyunin et al. (2017), the formation of methanol is most efficient in the "CO freeze-out zone" at densities of $n(H_2) \sim 10^4$–10^5 cm^{-3}, where the gas-phase abundance of CO is still high, a few times 10^{-5} relative to H_2. This model gives, therefore, an explanation for the fact that CH_3OH seems to avoid the densest parts and sometimes shows a shell-like distribution (Tafalla et al. 2006; Bizzocchi et al. 2014; Punanova et al. 2018).

The density of CO molecules in the CO-freezing zone is similar to that of H atoms, that is $n_{CO} \sim 1$ cm^{-3} ($X(CO) = 10^{-5}$–10^{-4}), but their average thermal speed is a factor of five lower, $\bar{v}_{CO} \sim 8700$ cm s^{-1}. Using the cross-sectional area of grains from the MRN size distribution and the CO flux implied by the density and the speed quoted above, the methanol production rate by reactive desorption is $\sim 4.3 \times 10^{-22}$ or 1.9×10^{-20} molecules s^{-1} per H atom (1.1×10^{-16} or 4.6×10^{-15} mol^{-1} s^{-1}), depending on whether we adopt $f_{CO} = 0.003$ or $f_{CO} = 0.13$. The higher of these rates is comparable to the cosmic-ray-induced sputtering rate of methanol from CO ice estimated in Section 6.1, based on the results of Dartois et al. (2019).

6.4. Grain–Grain Collisions Induced by Turbulence

As discussed by d'Hendecourt et al. (1982), low-velocity collisions between grains can lead to grain heating above the temperature threshold (~30 K) that triggers explosive radical–radical reactions and the partial disruption of the grain mantle. Assuming that the grains consist of a silicate core and a mantle of water ice constituting ~15% of the grain mass, one finds that the enthalpy change needed to raise the grain temperature from 10 to 27 K corresponds to a collision velocity of ~30 m s^{-1}. Here, we have adopted the heat capacity functions from Leger et al. (1985; their Equation (1)) and Shulman (2004; their Equation (4)) for the grain core and the ice mantle, respectively. The collisional speed that is needed to heat these grains to 100 K is 180 m s^{-1}.

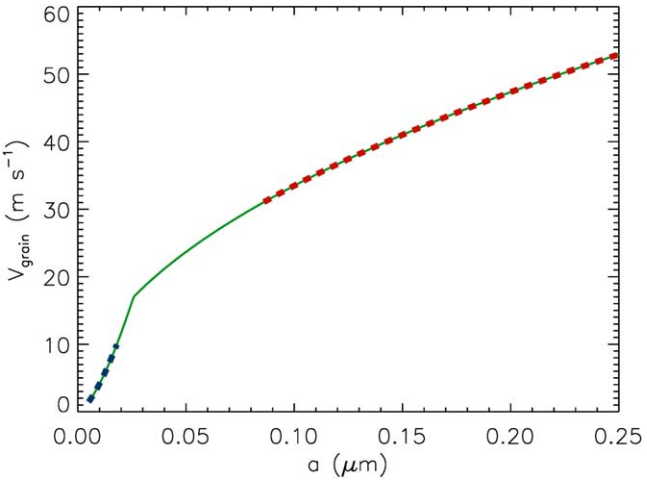

Figure 6. Relative speed of grains as a function of the grain radius according to the turbulent acceleration model (Draine 1985; Lazarian & Yan 2002) in dense dark cloud conditions (see the text). The regimes of "high" and "low" velocity grains are indicated with the thick dashed lines in red and blue, respectively. The discontinuity in the gradient is caused by the coupling of the smallest grains to the magnetic field. This occurs at $a = 0.026$ μm.

Collisions between grains require that the grain population has acquired an internal velocity dispersion. This can arise when grains are embedded in a turbulent gas (Voelk et al. 1978; Draine 1985). In the turbulent acceleration model presented by Draine (1985), the grain velocities are determined by turbulent velocity fluctuations occurring on a timescale comparable to that of the hydrodynamical drag. In Kolmogorov turbulence, the velocity is proportional to the square-root of the eddy turn-over time. Because the drag time is directly proportional to the grain radius, a, the velocity distribution of large grains has a square-root dependence on the grain radius, $v \propto a^{1/2}$. The smallest grains are also coupled to the magnetic field,[20] and their velocity dispersion is determined by turbulent fluctuations on a timescale comparable to the Larmor time (Lazarian & Yan 2002; Yan et al. 2004). This causes a $v \propto a^{3/2}$ dependence for the smallest grains. Overall, turbulent acceleration is more effective for large grains than for small grains. This gives rise to velocity differences between small and large grains and to an enhanced rate of grain–grain collisions.

In Figure 6, we show relative grain velocities as a function of grain radius according to the models of Draine (1985) and Lazarian & Yan (2002), for conditions characteristic of the outer envelope of a cold dense core, $n(H_2) = 10^5$ cm^{-3}, $T = 10$ K, $B = 100$ μG. Here, it is assumed that the turbulent velocity field has a Kolmogorov-like spectrum, $v \propto l^{1/3}$. The absolute scale is set by assuming that the turbulent velocity is 0.7 km s^{-1} on a scale of 0.034 pc. This corresponds to the velocity gradient across the H-MM1 core (Section 4; for discussion about the connection between velocity gradients and turbulence see Burkert & Bodenheimer 2000). Assuming the MRN grain size distribution, the small, slow grains with velocities below 10 m s^{-1} comprise ~50% of the total surface area of the grains, whereas the share of large, fast grains with $v > 30$ m s^{-1} is only ~5% of the surface area (albeit ~50% of the dust mass).

[20] A great majority of grains is negatively charged at visual extinctions above $A_V \sim 3^{mag}$ (Ivlev et al. 2015a).

The frequency at which a "slow" grain collides with a "fast" grain is obtained from

$$f_{\rm coll} = n_{\rm g}^{\rm fast}\ \pi(\bar{a}^{\rm fast} + \bar{a}^{\rm slow})^2\ (\bar{v}_{\rm g}^{\rm fast} - \bar{v}_{\rm g}^{\rm slow}), \quad (1)$$

where $n_{\rm g}^{\rm fast}$ is the number density of fast grains, $\bar{a}^{\rm fast}$ and $\bar{a}^{\rm slow}$ are the average radii of the fast and slow grains, respectively, $\bar{v}_{\rm g}^{\rm fast}$ and $\bar{v}_{\rm g}^{\rm slow}$ are their average speeds. Here, we have used the classical collisional cross section for hard spheres (e.g., Caselli et al. 1997). The MRN grain size distribution and the physical parameters mentioned above imply the following values for the average radii and speeds: $\bar{a}^{\rm slow} \sim 80$ Å, $\bar{a}^{\rm fast} \sim 0.12\ \mu$m, and $\bar{v}_{\rm g}^{\rm fast} - \bar{v}_{\rm g}^{\rm slow} \sim 34\ {\rm m\ s^{-1}}$. The number density of "fast" grains is $n_{\rm g}^{\rm fast} \sim 8 \times 10^{-8}\ {\rm cm^{-3}}$. With these parameters, the collision frequency is very low, $f_{\rm coll} \sim 1.4 \times 10^{-13}\ {\rm s^{-1}}$, meaning that a slow grain collides with a fast one once in ∼200,000 yr. Using the actual grain size and speed distributions without averaging, one obtains ∼25% higher grain–grain collision rate at a minimum speed difference of $30\ {\rm m\ s^{-1}}$.

When both particles are negatively charged, the kinetic energy overcomes the Coulomb barrier at this collision speed. We assume that a grain carries maximally one electron charge. The electrostatic repulsion can be important in collisions between the smallest grains with steep Coulomb potentials and small velocity fluctuations (Chokshi et al. 1993; Perez-Becker & Chiang 2011). In high-speed collisions, one of the grains is large, $a \sim 0.1\ \mu{\rm m} = 10^{-5}$ cm, and the minimum collision speed needed to overcome the Coulomb barrier is probably lower than the critical speed for sticking (Chokshi et al. 1993, Figure 8).

Despite the low collision frequency, the desorption rate can be high if every collision between a slow and a fast grain leads to a chemical explosion and the complete disruption of the ice mantle of the smaller, slow grain. In this case, the desorption rate of methanol would be $f_{\rm coll}\ n_{\rm CH_3OH}^{\rm surf,\ slow}$ molecules ${\rm cm^{-3}\ s^{-1}}$, where $n_{\rm CH_3OH}^{\rm surf,\ slow}$ is the number density of methanol molecules residing on slow grains (corresponding in our example to ∼50% of their total number density). It is, however, questionable if mild grain–grain collisions that heat small grains to ∼27 K can trigger mantle explosions, when these grains are, according to the results of Kalvāns (2018a), heated to the same temperature much more often by cosmic-rays (see end of Section 6.2), and the accumulation of radicals in the mantle is thereby inhibited.

Therefore, it seems plausible that only energetic grain–grain collisions that heat them close to ∼100 K can lead to significant desorption of methanol through thermal evaporation. The maximum grain speed acquired in Kolmogorov turbulence depends on the density and temperature according to $v_{\rm max} \propto n^{-1/2}\ T^{-1/4}$ (Draine 1985). At densities above $\sim 3 \times 10^5\ {\rm cm^{-3}}$, the maximum speed drops below the critical value $30\ {\rm m\ s^{-1}}$. Assuming that the temperature remains constant at 10 K, the maximum density where grain–grain collisions are energetic enough to heat them to 100 K (with a collisional speed of $\sim 180\ {\rm m\ s^{-1}}$) is $n({\rm H_2}) \sim 8 \times 10^3\ {\rm cm^{-3}}$. Grain–grain collision frequencies decrease toward lower densities, as is likely to happen to the methanol abundance on grains.

Following Shen et al. (2004; see their Equation (29)), we assume that collisional energy in excess of heating a grain to 26 K is available for sublimation. In a totally inelastic collision at $180\ {\rm m\ s^{-1}}$, this excess energy per unit mass is $\sim 16\ {\rm J\ g^{-1}}$. Adopting the mantle composition from Boogert et al. (2015) and assuming that the mantle constitutes 15% of the grain mass, the total binding energy of the mantle molecules per one gram of dust is $\sim 230\ {\rm J\ g^{-1}}$. Here, we have used the following binding energies: H_2O 5700 K, CO 1150 K, CO_2 2600 K, CH_3OH 5500 K, NH_3 5500 K, and CH_4 1300 K. So, it seems that the energy deposited by a grain–grain collision at $180\ {\rm m\ s^{-1}}$ can evaporate, at most, ∼7% of the mantle material. The minimum collision speed required for the evaporation of the whole mantle is $\sim 680\ {\rm m\ s^{-1}}$. Neglecting the differences in the binding energies, that is, assuming that the mantle species are evaporated in proportion to their relative abundances, we obtain a methanol desorption rate of $\sim 4 \times 10^{-21}\ {\rm s^{-1}}$ per H atom or $\sim 1 \times 10^{-15}\ {\rm mol^{-1}\ s^{-1}}$ at the density $n({\rm H_2}) \sim 8 \times 10^3\ {\rm cm^{-3}}$ (by collisions at the minimum speed of $180\ {\rm m\ s^{-1}}$). However, the presence of SO emission in the same region where we see CH_3OH lines in H-MM1 suggests that the density methanol desorption layer is of the order of $\sim 10^5\ {\rm cm^{-3}}$ (see Section 7). Kolmogorov turbulence at this density is unlikely to induce collisions leading to significant thermal evaporation.

6.5. Grain–Grain Collisions in a Shear Layer

The last mechanism discussed here is the release of methanol in grain–grain collisions induced by shear instability. This is motivated by the fact that the methanol distribution observed in H-MM1 (Figure 2) resembles Kelvin–Helmholtz clouds that sometimes develop in the atmosphere in flows with large vertical shears. As described in standard textbooks, such as Batchelor (1967), advection of vorticity amplifies the dominant sinusoidal disturbance in a vortex sheet and makes it roll up. The evolution of vortex sheets has been studied numerically and semi-analytically by Patnaik et al. (1976) and Corcos & Sherman (1976). According to their results, vorticity reaches its maximum values at places they call "braids" (near the troughs) and "cores" or cat's eyes (near the crests), separated by approximately half the wavelength of the dominant disturbance.

We conjecture that vorticity in the shear layer can accelerate dust grains to velocities deviating from the mean flow and induce grain–grain collisions, in the same manner as Kolmogorov-type turbulence discussed in the previous section. However, the energy spectrum and the corresponding velocity scaling law in a vortex sheet are different from those in fully developed turbulence (Kraichnan 1967, 1971; Gilbert 1988; Abid & Verga 2011).

The timescale of velocity fluctuations depends on the free-stream velocity and the size-scale of vorticity. The drag time for 0.1 μm grains is ∼100 yr at $n({\rm H_2}) \sim 10^5\ {\rm cm^{-3}}$. Assuming that the free-stream velocity is transonic, $U \sim 200\ {\rm m\ s^{-1}}$, one obtains that only small vortices of size $\lambda \lesssim 5$ au can give rise to significant velocity differences among the grain population.

In Figure 7, we plot the velocity field calculated from the stream function given by Corcos & Sherman (1976; their Equation (3.9)). Some of the streamlines are also plotted, including the so-called stagnation streamline, which outlines the cat's eyes. In this solution, the traverse time is not constant inside the cat's eyes but increases steeply from the center and reaches the maximum (∼300 yr in this example with $U = 200\ {\rm m\ s^{-1}}$, $\lambda = 10$ au) on the stagnation streamline.

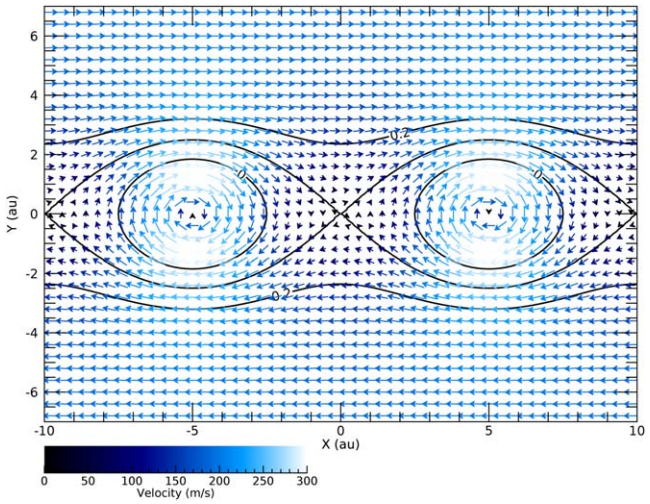

Figure 7. Velocity field in a periodic inviscid vortex sheet according to Corcos & Sherman (1976). Some of the streamlines, corresponding to the stream function values $\Psi = 0$, 0.1, and 0.2 times the maximum, are shown. The cat's eyes are outlined by the contour 0.1.

Beyond this streamline, the period of the smooth oscillatory motions attains quickly a constant value (∼230 yr).

In the structure shown in Figure 7, the turn-over time of the flow is shorter than the drag time of 0.1 μm grains within the contour $\Psi = 0$. One could expect grain–grain collisions to be concentrated to these regions, where small grains should be advected by the swirling flow, but large grains will not respond to the velocity fluctuations. For still smaller vortices, stagnation points between the cat's eyes (at the origin of Figure 7) are likely places of vigorous grain–grain collisions. Because of the high speed of the flow, the collisions are more frequent and more energetic than those induced by Kolmogorov turbulence. Assuming an average collision speed of 200 m s^{-1} and making the division between small and large grains at $a = 0.1$ μm, a small grain collides at an average frequency of $\sim 7 \times 10^{-13}$ s^{-1} (every 45,000 yr) at a density of $n(\mathrm{H_2}) \sim 10^5$ cm^{-3}. At this collision speed, the excess energy after heating the grains to 26 K is ∼20 J g^{-1}, and we assume that this is sufficient for evaporating 9% of the mantle material (see end of Section 6.4).

The resulting methanol desorption rate is $\sim 3 \times 10^{-14}$ molecules cm^{-3} s^{-1} or $\sim 2 \times 10^{-19}$ s^{-1} per H atom, corresponding to $\sim 4 \times 10^{-15}$ mol^{-1} s^{-1}. Here, we have again assumed that the fractional abundance of methanol ice is 4×10^{-6} with respect to H atoms. The desorption rate by shear-induced grain–grain collisions is comparable to the rates of reactive desorption and cosmic-ray-induced sputtering in their upper ranges. This mechanics is, however, confined to very small volumes near discontinuities in the velocity field. Assuming that the vortex sheet is linear with a thickness of 5 au, it fills approximately 1% of the 560 au beam of the present observations. A winding structure would increase the beam filling factor slightly. Nevertheless, taking the nonuniform beam filling into account, the contribution of grain–grain collisions in shear layers to the observed methanol abundance can be locally similar to those of the more widespread reactive desorption and cosmic-ray-induced sputtering. The estimated methanol desorption rates for different mechanisms are summarized in Table 2.

Table 2
Estimated CH_3OH Desorption Rates and the Sections Where They Are Discussed

Mechanism	k_{des} (mol^{-1} s^{-1})	Section
Cosmic-ray desorption	6×10^{-17}–2×10^{-15}	6.1
Photodesorption	4×10^{-18}–8×10^{-17}	6.2
Reactive desorption	$1 \times 10^{-16} - 5 \times 10^{-15}$	6.3
Grain–Grain collisions		
Kolmogorov turbulence	$\sim 1 \times 10^{-15}$[a]	6.4
Shear instability	$\sim 4 \times 10^{-15}$[b]	6.5

Notes.
[a] Unlikely to work at high densities.
[b] Localized to small areas.

7. Origin of Gaseous Methanol in H-MM1

In accordance with previous mappings toward L1544 (Bizzocchi et al. 2014; Spezzano et al. 2017; Punanova et al. 2018), we find relatively high abundances of methanol in a prestellar core, offset from the density maximum. With ALMA, the methanol distribution in H-MM1 could be mapped with a higher spatial resolution than achieved in L1544, and it was found to be confined to a layer that follows the core boundaries. The apparent thickness of this layer is of the order of 1000 au, except for the bright curved feature at the southeastern boundary that is unresolved with our 560 au beam. The critical density of the coexistent SO($3_2 - 2_1$) line is 3×10^5 cm^{-3} at 10 K, whereas for the methanol lines, this is 3×10^4 cm^{-3}. We assume that the higher of these values, $\sim 10^5$ cm^{-3}, is characteristic of the gas component detected in CH_3OH and SO. This value agrees with the densities derived by Bacmann & Faure (2016) for methanol emission regions in prestellar cores. At still higher densities, traced by NH_2D, both CH_3OH and SO are apparently frozen out.

Sulphur monoxide can form both in the gas phase and on grain surfaces. Without efficient desorption, gaseous SO depletes quickly at high densities. On the other hand, as soon as atomic sulfur is available, SO and other sulfur-bearing molecules are thought to form quickly in the gas phase through reactions with O, O_2, and OH (Fuente et al. 2016; Vidal et al. 2017). According to modeling results of Laas & Caselli (2019), the principal sulfur-bearing species in the ice at advanced chemical stages are SO, OCS, HSO, and CS. Also, pure-sulfur molecules, in particular S_8, have been suggested to be abundant on grains (Shingledecker et al. 2020). Methanol and sulfur monoxide are not directly related. Their spatial coincidence could possibly be explained by co-desorption of CH_3OH and SO or sulfur in some other form. Alternatively, gas-phase reactions forming SO may be efficient in the same conditions where CH_3OH is desorbed.

According to the estimates presented in the previous section, the efficiencies of reactive desorption and desorption in grain–grain collisions in the presence of vigorous velocity fluctuations can be comparable to the efficiency of direct cosmic-ray-induced desorption, but the two mechanisms mentioned first are likely to be spatially limited to certain zones of a cloud. The reactive desorption model predicts that the CH_3OH and SO abundances peak on the outskirts of a dense core (Vasyunin et al. 2017, their Figures 4 and 8). In this model, gaseous methanol is abundant at a depth where water is partially photodissociated (Figure 6 of Vasyunin et al. 2017). The presence of hydrogen atoms and hydroxyl radicals in this layer

can also promote the formation of SO in the gas phase. On the other hand, if methanol formation is most efficient in the CO-freezing zone, a halo-like structure does not depend on the actual desorption mechanism. Also, cosmic-ray-induced desorption can be thought to give rise to a similar distribution, especially if one takes the reduction of cosmic-ray flux toward the interior parts into account (Padovani et al. 2009; Ivlev et al. 2015b).

The strong asymmetry observed in H-MM1 is, however, difficult to explain without invoking an external agent, which either destroys CH_3OH and SO on one side of the core or creates them on the opposite side through forceful desorption. We first discuss the possible effect of an asymmetric radiation field.

7.1. Uneven Illumination

An asymmetric methanol distribution has been previously found in the prestellar core L1544 (Spezzano et al. 2016; Punanova et al. 2018). Spezzano et al. (2016) suggested that the methanol distribution in L1544 reflects asymmetric illumination, which hinders CO production on the more exposed side of the cloud. Intense radiation could also inhibit SO formation by ionization. The ionization potentials of SO and the S atom are relatively low, 10.29 eV and 10.36 eV, respectively; the limiting wavelength of ionizing radiation, $\lambda < 120$ nm, falls in the range where photons also can dissociate CH_3OH efficiently (114 nm $< \lambda <$ 180 nm; Cruz-Diaz et al. 2016).

The ambient cloud around H-MM1 continues toward the east, giving reason to believe that the interstellar radiation field is stronger on the western side where CH_3OH and SO are weaker. This side faces the Upper Sco-Cen subgroup of the Scorpius-Centaurus OB association, including the luminous B-type double stars ρ Oph and HD 147889 (de Geus 1992; Preibisch & Mamajek 2008; Damiani et al. 2019). The blue subgiant binary HD 147889, about 1.2 pc west of H-MM1, is the dominant UV source in the region (Liseau et al. 1999; Casassus et al. 2008; Rawlings et al. 2013).

If the radiation field is stronger on the western side, this should be evident as a dust temperature difference between the two sides of the core because dust grains are primarily heated by absorption of starlight. We examined this hypothesis using mid- to far-infrared maps from Spitzer, Herschel, and SCUBA-2, and we found that the dust temperature reaches, indeed, its minimum on the eastern side of the core, close to the CH_3OH maximum. The analysis of the dust continuum maps is presented in Appendix B. The analysis suggests a temperature drop from about 14–15 K on the western edge to about 11–12 K in the eastern cove of the core (see Figure B1).

We tested this result by simulating the effect of an asymmetric radiation field on a core model resembling H-MM1. The strength of the external field was adjusted until the model could reproduce the observed surface brightness maps at 850 μm. The details of the calculation are presented in Appendix B. The simulation shows that an anisotropic radiation field causes a displacement of the temperature minimum from the density maximum and that this displacement can be inferred by comparing 70 and 850 μm surface brightness maps. It also gives estimates for the strength of the FUV radiation field on the eastern and western edges of the core. The energy density of the FUV field along three cuts across the model core is shown in Figure B2. The strongest methanol emission in H-MM1 is found at the offsets 10″–20″ east of the density maximum (the map center). In the simulated core, the FUV energy density has a deep minimum in this range, and the average radiation flux originating from the external field is negligible. In the corresponding region on the western side of the core, the average FUV flux is approximately $F_{\rm FUV} = 80{,}000$ photons cm^{-2} s^{-1}, that is, an order of magnitude higher than the flux of cosmic-ray-induced photons ($F_{\rm FUV} = 5000$ cm^{-2} s^{-1}) in dense dark clouds estimated by Cecchi-Pestellini & Aiello (1992).

The difference in the FUV fluxes at the western and eastern boundaries of the core is likely to affect the methanol abundances both in the gas and on grains. Assuming that CH_3OH is formed on grains through CO accretion and removed by photodissociation and by some generic desorption mechanism, its equilibrium abundance on grains relative to H atoms can be written as

$$X(\mathrm{CH_3OH, s}) = \frac{f_{\rm CO}\,\sigma_{\rm H}\,\bar{v}_{\rm CO}\,n_{\rm CO}}{\sigma_{\rm ph,s}\,F_{\rm FUV} + k_{\rm des}}, \quad (2)$$

where $f_{\rm CO}$ is the efficiency factor for the conversion CO $\rightarrow$ CH_3OH on grains, $\bar{v}_{\rm CO}$ is the average thermal speed of CO molecules, $n_{\rm CO}$ is their number density, $\sigma_{\rm ph,s} = 2.7 \times 10^{-18}$ cm^2 is the FUV photodissociation cross section of methanol ice (Cruz-Diaz et al. 2016), and $k_{\rm des}$ is the desorption rate per molecule s^{-1}. We assume here that the desorption rate is constant and represents the high end of the various estimates above, that is, $k_{\rm des} = 5 \times 10^{-15}$ mol^{-1} s^{-1}. For simplicity, we also assume the number density and the average speed of CO molecules are constant in the core, $n_{\rm CO} = 1$ cm^{-3}, $\bar{v}_{\rm CO} = 8700$ cm s^{-1}. Moreover, we assume that a constant cosmic-ray-induced FUV flux, 5000 cm^{-2} s^{-1}, comes everywhere on top of the attenuated external field. We then adjust the efficiency factor $f_{\rm CO}$ so that the maximum fractional methanol abundance on grains is 4×10^{-6}. The resulting factor is $f_{\rm CO} = 0.05$.

Assuming that accretion onto grains and photodissociation dominate the destruction of gas-phase methanol, its equilibrium abundance can be obtained from

$$X(\mathrm{CH_3OH, g}) = \frac{X(\mathrm{CH_3OH, s})\,k_{\rm des}}{n_{\rm H}\,\sigma_{\rm H}\,\bar{v}_{\rm CH_3OH} + \sigma_{\rm ph,g}\,F_{\rm FUV}}, \quad (3)$$

where $\bar{v}_{\rm CH_3OH}$ is the average thermal speed of methanol molecules ($\sim$8100 cm s^{-1} at 10 K), and $\sigma_{\rm ph,g}$ is the FUV photodissociation cross section of methanol in the gas. For the latter, we adopt the value $\sigma_{\rm ph,g} \sim 1 \times 10^{-17}$ cm^2 based on the experimental results of Person & Nicole (1971) and Cheng et al. (2002). The hydrogen density, $n_{\rm H}$, comes from our core model. The grain-surface and gas-phase abundances of methanol calculated from Equations (2) and (3) along a horizontal line that goes through the density maximum of the core model are plotted in Figure 8. The abundance profile in the gas phase is double-peaked, with the stronger peak residing on the dark side of the core, whereas on grains, the abundance profile is flat-topped. The eastern and western gas-phase peaks, with $X(\mathrm{CH_3OH, g}) \sim 4 \times 10^{-9}$ and $X(\mathrm{CH_3OH, g}) \sim 3 \times 10^{-9}$, occur at the densities $n(\mathrm{H_2}) \sim 1.8 \times 10^5$ cm^{-3} (east) and $n(\mathrm{H_2}) \sim 2.0 \times 10^5$ cm^{-3} (west). The fractional grain-surface methanol abundances at

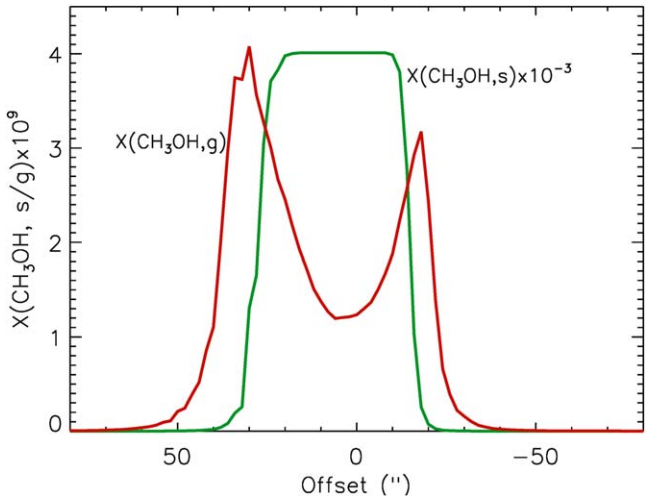

Figure 8. Fractional methanol abundances on grain (s) and in the gas (g) relative to H atoms as functions of distance from the core center. The abundances are calculated using Equations (2) and (3) together with the FUV flux and particle density from our three-dimensional model of H-MM1. The offsets are measured along a line lying in the plane of the sky.

these locations are $X(\mathrm{CH_3OH, s}) \sim 1.3 \times 10^{-6}$ (east) and $X(\mathrm{CH_3OH, s}) \sim 2.6 \times 10^{-7}$ (west). The stronger methanol peak lies much farther out from the core center than in the observed core, but we cannot exclude the possibility that the difference is caused by a projection effect.

This simple model can be envisaged to give a qualitative explanation for the methanol distribution observed in H-MM1, even though Figure 8 shows the methanol abundance along a line lying in the plane of the sky, while we are measuring line-of-sight averages. However, the contrast between the peak methanol abundances on the eastern and western sides, $\gtrsim$10:1, cannot be reproduced by this model. Increasing the external FUV flux would shift the methanol peaks inward, toward higher densities, but the abundance ratio would remain the same, approximately 4:3. Likewise, one can increase or decrease the gas-phase abundances by adjusting the desorption rate with the same effect on the abundance ratio.

Other than indicating asymmetry in the radiation field, the dust temperature drop itself can contribute to the high abundances of CH_3OH on the eastern side. Methanol production is probably favored by efficient accretion and hydrogenation of CO on grains at low temperatures. It should be noted, however, that the cooler region does not cover the whole eastern side of the core where strong CH_3OH emission is found, and it does not extend to the SO maximum. At the northern and southern ends of the integral-shaped CH_3OH and SO emission region, the dust temperature is similar to that on the western side where these species show only weak emission.

The estimates and considerations presented above suggest that in addition to the fact that the H-MM1 core is exposed to a strong, asymmetric radiation field that hinders methanol formation on its western side, desorption is particularly effective at its eastern boundary. Of the mechanisms discussed in Section 6, photodesorption is very unlikely to cause this effect. Also, it is not likely that the cosmic-ray flux shows substantial anisotropy on this scale or that the efficiency of reactive desorption is higher in the east, except perhaps in the vicinity of the temperature minimum (Appendix B). In what follows, we therefore consider desorption related to gas dynamics at the core boundaries.

7.2. Shocks

Both CH_3OH and SO are known to increase in shocks, and they have been used to probe outflows and the accretion process associated with star formation (Bachiller & Pérez Gutiérrez 1997; Podio et al. 2015; Oya et al. 2016). Strong enhancement of SO and SO_2 is predicted by models of magnetized molecular C-shocks, as a result of neutral–neutral reactions in the shock-heated gas and the erosion of S-rich icy grain mantles owing to bombardment by heated gas particles (Pineau des Forêts et al. 1993; Flower & Pineau des Forets 1994). Sputtering of the grain mantles associated with shocks can also increase the CH_3OH abundance substantially in the gas phase (Jiménez-Serra et al. 2008). Previous observations of mid-J CO rotational lines toward Perseus and Taurus complexes suggest low-velocity shocks associated with dissipation of turbulence and core formation in molecular clouds (Pon et al. 2014; Larson et al. 2015). Judging from the fact that the nonthermal velocity dispersion experiences an abrupt change at the core boundary (Auddy et al. 2019; see Section 7.3), low-velocity shocks caused by accreting material are also possible in the case of H-MM1. However, the present data consisting of low-lying rotational lines CH_3OH, SO, and NH_2D do not show any evidence of shock heating or velocity gradients that would be large enough ($\Delta v \gtrsim 10$ km s^{-1}) to give rise to significant shock-induced sputtering (Caselli et al. 1997; Jiménez-Serra et al. 2008).

7.3. Desorption in the Turbulent Envelope

The interior parts of the H-MM1 core have a very low level of nonthermal motions. This is evident from the velocity dispersion of the ortho-NH_2D lines illustrated in Figures 4(a) and (5). In a study based on NH_3(1, 1) and (2, 2) inversion line observations from the GAS (Friesen et al. 2017), Auddy et al. (2019) show that the nonthermal velocity dispersion increases suddenly at the boundaries of this and several other cores in Ophiuchus. Turbulent acceleration of grains and grain–grain collisions can be envisioned to lead to an enhanced desorption of frozen molecules in the transition zone. The process should affect all atoms and molecules residing in the CO-rich outer layers of grain mantles, and this would explain why CH_3OH and SO have similar distributions.

In this scenario, the asymmetric distributions of CH_3OH and SO around H-MM1 would either indicate that turbulence is stronger on the eastern side of the core or that dust grain surfaces are richer in CO on that side. The latter suggestion is supported by the fact that the CH_3OH peak coincides with the dust temperature minimum (Appendix B). The former condition cannot be properly tested using the present data because the boundaries are not probed with any other lines than methanol and SO; the NH_2D line emission is confined to the inner regions where the lines are narrow. The angular resolution of the Green Bank NH_3 maps (32″; Friesen et al. 2017), which cover both the core and the ambient cloud, is not sufficient for detailed comparison of the velocity dispersions at the eastern and western boundaries. Nevertheless, a similar analysis as performed by Auddy et al. (2019), but averaging over semicircles shows that the nonthermal velocity dispersion (measured along the line of sight) grows more slowly on the

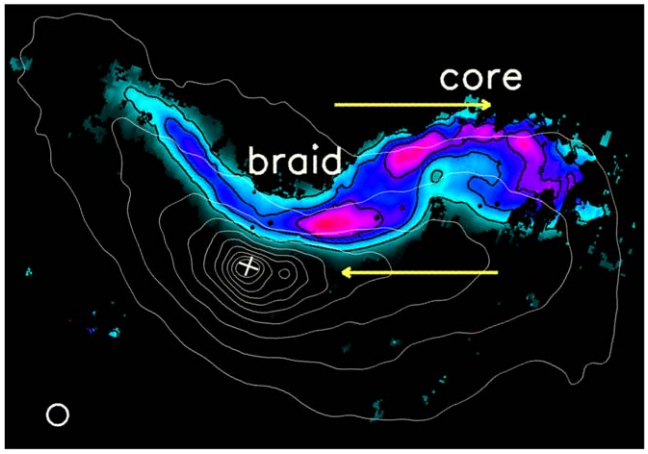

Figure 9. Maps of the fractional $E-CH_3OH$ abundance and the H_2 column density (contours) already shown in Figure 2 but rotated here by 110°. The arrows indicate the hypothesized flow directions in the denser and thinner gas components, relative to the average speed of the flow. The arrow length, 30″, corresponds approximately one-half the length of the wave-like structure.

eastern side than on the western side, contradicting the supposition of a more vigorous turbulence on that side. A diagram illustrating this difference is shown in Figure C1.

7.4. Desorption in a Shear Layer

One remarkable feature of the brightest CH_3OH emission region is that it closely follows the eastern boundary of the core as marked by NH_2D emission. The wavy shape and the rolling-up seen in the north (Figure 2) are the hallmarks of Kelvin–Helmholtz instability (KHI), which can occur in sheared flows with density stratification. The channel maps shown in Figure 3 give the impression that the dense gas is flowing along a loop. If the ambient gas does not share this motion, the core is surrounded by a shear layer. The presence of shear in a gas flow with a high Reynolds number would imply small-scale vorticity, and the undulating methanol emission region would, in this case, consist of a chain of secondary billows that are unresolved in the present map. In this scenario, the methanol peak can be identified with a "braid" with crowded isopycnic surfaces and the overturning billow in the north with a "core" where these surfaces roll up (Patnaik et al. 1976; see Section 6.5). The apparent wavelength of the methanol feature is approximately 60″, corresponding to 8400 au or 0.041 pc. The conceived structure is illustrated in Figure 9, which shows the maps of Figure 2 rotated in such a way that the suggested shear layer is approximately horizontal and the density increases downward. The directions of the relative velocities of the denser and thinner gas components are shown with arrows, and the positions of the "braid" and "core" are indicated.

In what follows, we attempt to estimate the flow properties, assuming that, analogously to atmospheric billow clouds, the largest wavelength corresponds to the so-called internal gravity waves, which oscillate at the Brunt–Väisälä frequency. This frequency, also known as the buoyancy frequency, is defined by $N=\sqrt{\frac{-g}{\rho}\frac{\partial\rho}{\partial z}}$, where g is the gravitational acceleration (directed to the negative z-direction), and ρ is the gas density. We estimated the density and the density gradient in the supposed shear layer by fitting a Plummer-type function to the H_2 column density profile from the IRAC 8 μm absorption. The inversion method is explained by Arzoumanian et al. (2011).

The fit was made to the cross-sectional profile along an axis going through the methanol peak at R.A.16:27:59.5, decl. −24:33:30 (J2000). The axis is tilted with respect to the R.A. axis by 25°. According to this fit, the number densities at the methanol peak and at the spine of cloud are $\sim 3.8\times10^5$ cm^{-3} and $\sim 9.2\times10^5$ cm^{-3}, respectively. The separation between these points is approximately 10″ (1400 au). We assumed that the gravitational field at the methanol peak is dominated by the mass contained in a circular region of a radius of 10″, centered at the crossing of the cloud spine and the cross-sectional axis. This mass is 0.11 $M_\odot$. The Brunt–Väisälä frequency obtained is $N\sim 1.3\times10^{-12}$ Hz (period 150,000 yr). The multiplication of N by the apparent wavelength gives a phase velocity of $\sim$260 m s^{-1}. This should correspond to the average speed of the sheared flow.

In the case that the flow is subject to KHI, a condition is imposed to the velocity shear: the Richardson number, defined by $\mathrm{Ri}=\frac{N^2}{(\partial v/\partial z)^2}$, is less than one-fourth. The implied minimum shear is $\sim 2.6\times10^{-12}$ s^{-1} or $\sim$80 km s^{-1} pc^{-1}. This value exceeds the north–south velocity gradient derived from the molecular line maps by a factor of four. Assuming that the velocity at the outer boundary of the shear layer does not exceed 400 m s^{-1}, which is the typical nonthermal velocity far from the core, the maximum thickness of the layer is approximately 1000 au. This estimate agrees with the thickness of the methanol layer.

In view of the uncertainties concerning the "vertical" scale and the structure of the vorticity, we do not attempt to estimate the methanol production rate in the suggested vortex sheet. We merely state that the present observations indicate that the formation of methanol is more efficient in this layer than elsewhere in the core envelope. We suggest, based on the theoretical and numerical studies quoted above, that this is caused by the fact that two-dimensional turbulence can have larger velocity fluctuations than full three-dimensional turbulence on a timescale comparable to the drag time of dust grains.

8. Conclusions

Gaseous methanol and sulfur monoxide coexist on the outskirts of the prestellar core H-MM1 in Ophiuchus. They are confined to a halo that follows the core boundaries and that is particularly prominent on the eastern side of the core. Because methanol is mainly produced on grains, the emission indicates regions of enhanced desorption. Sulphur monoxide may have co-desorbed with CH_3OH or formed in the gas phase following the release of other S-bearing species. The distribution of deuterated ammonia, NH_2D, follows the H_2 column density distribution and is almost complementary to those of CH_3OH and SO. This can be understood by the fact that deuterium fractionation is most efficient in the gas component where CO and other heavier species are strongly depleted, which is equivalent to ineffective desorption.

The asymmetry of the CH_3OH and SO distributions is partly caused by the strong, uneven illumination of the core, which mainly comes from luminous B-type stars on its western side. Our radiative transfer calculations indicate that the FUV field, albeit heavily attenuated, is significantly stronger on the western boundary of the core, with weak CH_3OH and SO emission, than on the eastern boundary, where these molecules

emit strongly. The asymmetric FUV field has two effects: first, the photodissociation rate of CH_3OH is higher on the western side. Second, the dust temperature has a minimum on the eastern side of the core. The minimum coincides with the methanol maximum. This is understandable as CO accretion and hydrogenation are favored at low temperatures.

We suggest that external radiation is not the sole factor causing the contrast between the CH_3OH and SO abundances on the two sides of the core but that this contrast is increased by forceful desorption on its shaded, eastern boundary. We consider it possible that grain–grain collisions make a significant contribution to desorption, along with cosmic-ray collisions and spontaneous exothermic surface reactions. Desorption by grain–grain collisions can proceed through mild heating that triggers explosive radical–radical reactions and partial disruption of grain mantles (d'Hendecourt et al. 1982), or through direct heating in energetic collisions. Collisions between grains can be induced by Kolmogorov turbulence (Draine 1985; Lazarian & Yan 2002), or by shear vorticity.

The brightest methanol emission region at the eastern boundary of the core shows signatures of KHI, indicating strong velocity shear. On the other hand, the nonthermal velocity dispersion along the line of sight, as traced by NH_3 lines, grows more steeply on the opposite side of the core, where both CH_3OH and SO emissions are weak. We interpret this so that at the eastern boundary, laminar flow occurring mainly in the plane of the sky is currently transitioning into turbulence through shear instability, whereas on the western side, the flow has already developed into full three-dimensional turbulence. The asymmetries of the CH_3OH and SO distributions suggest that shear vorticity induces more energetic or more frequent grain–grain collisions than Kolmogorov turbulence. This is likely to be related to the fact that two-dimensional turbulence has a steeper energy spectrum (Kraichnan 1971), implying larger velocity fluctuations on the timescale needed to accelerate grains through hydrodynamic drag.

We thank Tom Hartquist, David Williams, Kalevi Mattila, and Hannu Savijärvi for helpful and enjoyable conversations, and the anonymous referee for critical comments that helped to improve this paper. The paper makes use of the following ALMA data: ADS/JAO.ALMA#2016.1.00035.S. ALMA is a partnership of ESO (representing its member states), NSF (USA) and NINS (Japan), together with NRC (Canada), MOST and ASIAA (Taiwan), and KASI (Republic of Korea), in cooperation with the Republic of Chile. The Joint ALMA Observatory is operated by ESO, AUI/NRAO and NAOJ. The National Radio Astronomy Observatory is a facility of the National Science Foundation operated under cooperative agreement by Associated Universities, Inc.

This work is based in part on observations made with the Spitzer Space Telescope, and made use of the NASA/IPAC Infrared Science Archive. These facilities are operated by the Jet Propulsion Laboratory, California Institute of Technology under a contract with National Aeronautics and Space Administration. This work was supported by the Academy of Finland (grants 285769 and 307157). Work by A.V. and A.P. is supported by Russian Science Foundation via the Project 18-12-00351. A.V. and A.P. are members of the Max Planck Partner Group at the Ural Federal University.

Appendix A
Column Density Map from 8 μm Extinction

The core is largely obscured from ultraviolet radiation and it serves as an absorbing component at 8 μm. The surface brightness in the core region can therefore be written as $I^{8\,\mu\mathrm{m}} = I_{\mathrm{bg}}^{8\,\mu\mathrm{m}}\, e^{-\tau^{8\,\mu\mathrm{m}}} + I_{\mathrm{fg}}^{8\,\mu\mathrm{m}}$, where $\tau^{8\,\mu\mathrm{m}}$ is the optical thickness at 8 μm, I_{bg} is the surface brightness at the background of the core, and I_{fg} is the surface brightness of the foreground component (see, e.g., Butler & Tan 2009). The latter term may also contain a zero-point offset. The optical thickness map can be obtained from

$$\tau^{8\,\mu\mathrm{m}} = -\ln\left\{\frac{I^{8\,\mu\mathrm{m}} - I_{\mathrm{fg}}^{8\,\mu\mathrm{m}}}{I_{\mathrm{bg}}^{8\,\mu\mathrm{m}}}\right\}.$$

In order to estimate the background emission, $I_{\mathrm{bg}}^{8\,\mu\mathrm{m}}$, we made a fit to the surface brightness distribution with the core masked out. For masking, we used the SCUBA-2 850 μm map. The foreground component, $I_{\mathrm{fg}}^{8\,\mu\mathrm{m}}$ (including possible zero-point offset), was assumed to be constant in the mapped region. Its value was estimated by requiring that the ratio of the peak optical thicknesses is $\tau^{8\,\mu\mathrm{m}}/\tau^{850\,\mu\mathrm{m}} = 780$, corresponding to the adopted dust opacity model, which was the model for unprocessed dust grains with thin ice mantles by Ossenkopf & Henning (1994). The comparison was done using an IRAC map smoothed to the resolutions of the SCUBA map.

At 850 μm, the core is optically thin, and it is seen in thermal dust emission. The observing method filters out extended emission. The surface brightness is therefore $I^{850\,\mu\mathrm{m}} = B^{850\,\mu\mathrm{m}}(T_{\mathrm{d}})\tau^{850\,\mu\mathrm{m}}$, where T_{d} is the dust temperature and B is the Planck function. The opacity map at 850 μm, $\tau^{850\,\mu\mathrm{m}}$, was calculated by combining the 850 μm surface brightness map with the dust color temperature map, T_{C}, derived from Herschel/SPIRE maps (Harju et al. 2017). The angular resolution of the T_{C} map is $\sim$40″, whereas for SCUBA, it is approximately 14″. We think this discrepancy in the angular resolutions is acceptable because the 850 μm surface brightness is not very sensitive to the dust temperature (see below).

Finally, the H_2 column density map shown in Figure 1(d) was calculated by dividing the 8 μm optical thickness map by the absorption cross section of dust per H_2 molecule, which, according to the adopted dust model, is 4.1×10^{-23} cm^2 H_2 molecule^{-1} (8.86 cm^2 g^{-1}).

Appendix B
Dust Temperature Distribution

At 70 μm, a cloud can be seen either as deficiency or excess of surface brightness depending on the dust temperature and the brightness of the background. At this wavelength, the Planck function is very sensitive to small changes in the temperature. For example, a temperature change from 12 to 14 K for a given dust column increases the emission by an order of magnitude, while at 850 μm, the corresponding change is $\sim$20%. The surface brightness at 70 μm takes the form

$$I^{70\,\mu\mathrm{m}} = I_{\mathrm{bg}}^{70\,\mu\mathrm{m}}\, e^{-\tau^{70\,\mu\mathrm{m}}} + I_{\mathrm{fg}}^{70\,\mu\mathrm{m}} + B^{70\,\mu\mathrm{m}}(T_{\mathrm{d}})(1 - e^{-\tau^{70\,\mu\mathrm{m}}}).$$

We assumed that the $\tau^{70\,\mu\mathrm{m}}$ distribution is identical to that at 8 μm, save for a constant factor depending on the adopted dust opacity model for large "classical" grains (giving

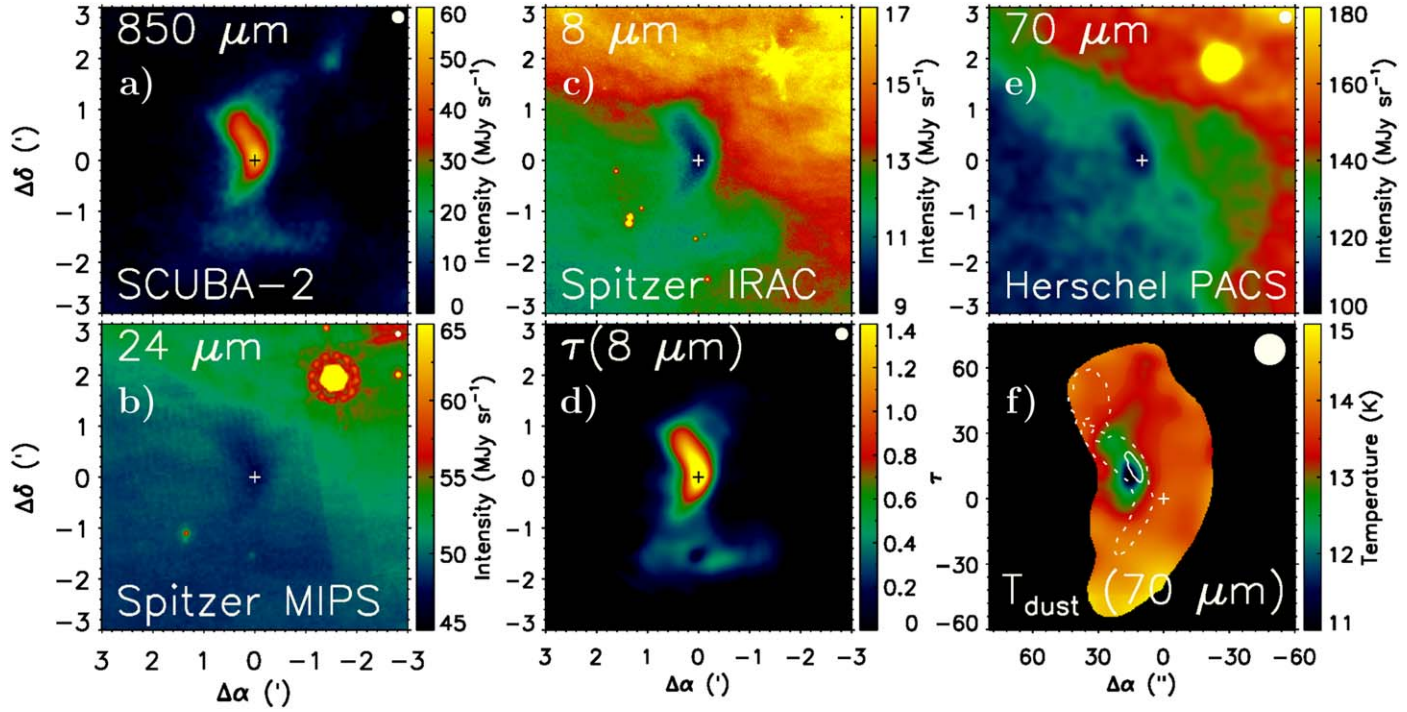

Figure B1. Surface brightness maps of H-MM1 at selected mid- to far-infrared wavelengths (panels (a) to (d)), and the optical thickness (e) and the dust temperature (f) maps derived from these. The instruments and wavelengths are indicated in panels (a) to (d). The optical thickness map in panel (d), $\tau^{8\,\mu\mathrm{m}}$, is derived from the Spitzer/IRAC map at 8 μm. The dust temperature map, T_{dust}, in panel (f) is derived using the Herschel/PACS map at 70 μm. Note that in this method, T_{dust} can be only derived when $\tau^{70\,\mu\mathrm{m}}$ is finite, and the region shown is smaller than in other panels. The maps presented in panels (d), (e), and (f) are smoothed to the angular resolution of the SCUBA map in panel (a) (14″). The maps in panels (b) and (c) are shown at the original resolutions, 6″ and 2″, respectively. The angular resolution is indicated with a filled circle in the top right. The region of bright CH_3OH emission is outlined with dashed and solid contours in panel (f). The plus sign indicates the position of the H_2 column density maximum.

$\tau^{8\,\mu\mathrm{m}}/\tau^{70\,\mu\mathrm{m}} = 1.2$). The foreground level (including a possible zero-point offset) was adjusted so that the dust temperatures on the outskirts of the core are similar to T_{C} values derived from Herschel/SPIRE. The obtained dust temperature distribution in the core region is shown in the bottom right panel of Figure B1. For the T_{d} calculation, the 8 and 70 μm maps were smoothed to the 14″ resolution of the SCUBA-2 map.

This map indicates that the dust temperature minimum is located on the eastern side of the column density maximum and is nearly coincident with the CH_3OH maximum. We tested this result by constructing a core model resembling H-MM1. In the plane of the sky, the cloud structure was taken from the observed 850 μm optical depth map, and the line-of-sight density distribution has the same shape as the $\tau^{850\,\mu\mathrm{m}}$ profile along horizontal cuts across the core. The core was illuminated by an isotropic radiation field plus a point source located on its western side. The dust opacity model was the same as that used above. The calculations were done using the dust continuum radiative transfer program described in Juvela (2019). The isotropic field was set equal to 30 times the Mathis et al. (1983) field, and the luminosity of point source (modeled as a 10,000 K blackbody) was selected so that its contribution to the radiation field at the cloud center was equal to that of the isotropic background. The combined strength of the isotropic component and the point source were then adjusted until the 850 μm surface brightness map agreed with the observations.

The dust temperature distribution derived from the simulated 70 μm map in the same manner as described above shows a similar shift of the minimum as seen in Figure B1(f). In the "true," three-dimensional distribution, the dust temperature minimum is shifted to the same direction but lies a little closer to the density peak. This experiment shows that dust temperatures derived from the 70 μm surface brightness temperature map can correctly reflect, although exaggerating slightly, the displacement of the dust temperature minimum from the density maximum (and the 850 μm peak) caused by anisotropic illumination. Figure B2 shows the energy density of the 6.0–13.6 eV UV radiation field for one-dimensional cuts through the densest part of the model. The energy density is plotted as G_0, relative to the Habing value of 5.29×10^{-14} erg cm^{-3} (Habing & Israel 1979).

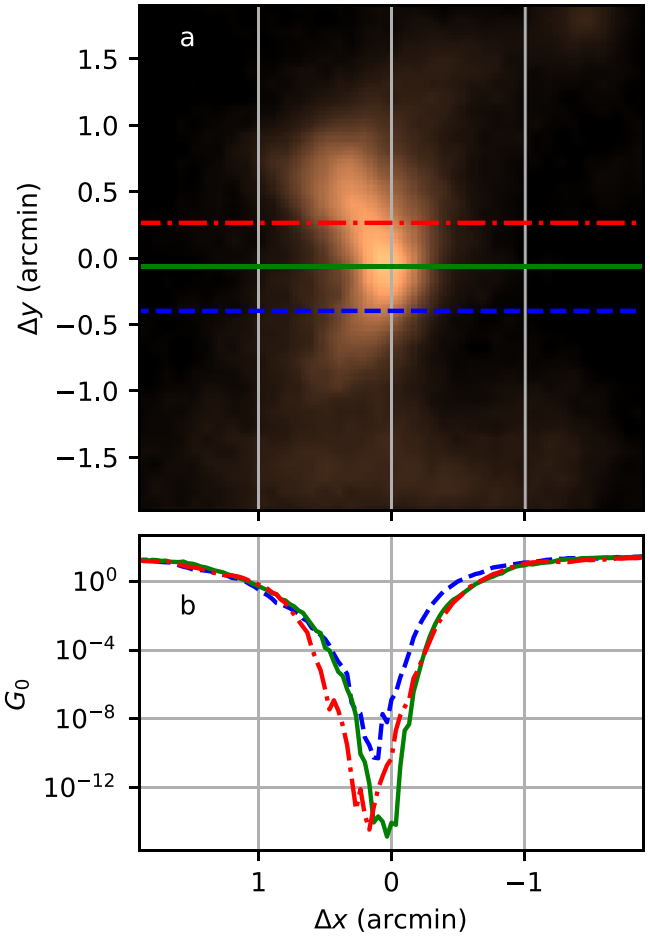

Figure B2. Strength of the UV radiation field inside the model cloud. Frame (a) shows the locations of three horizontal cuts, drawn on a map of the 850 μm optical depth. Frame (b) shows the 6.0–13.6 eV energy density along those lines, relative to the Habing field.

Appendix C
Velocity Dispersion Profiles

Thermal and nonthermal velocity dispersion profiles on the eastern and western sides of the core were calculated using NH_3(1, 1) and (2, 2) inversion line data from the GAS (Friesen et al. 2017). The method is described in detail by Auddy et al. (2019). The spectra were first aligned in velocity using the Green Bank pipeline-reduced LSR velocity maps and then averaged in concentric semiannular regions. The stacked NH_3(1, 1) and (2, 2) spectra were analyzed using the standard method described, for example, by Ho & Townes (1983). This analysis gives estimates for the kinetic temperature and total velocity dispersion (along the line of sight). The radial distributions of thermal and nonthermal velocity dispersions were calculated from these data. The results for the two hemispheres of H-MM1 are shown in Figure C1. The nonthermal dispersion is approximately half the sound speed near the center, and reaches a value of $\sim$400 m s^{-1}, that is, twice the sound speed far from the center of the core. The transition from subsonic to supersonic regimes occurs, however, closer to the center on the western side of the core than the eastern side, where the strongest methanol emission comes from.

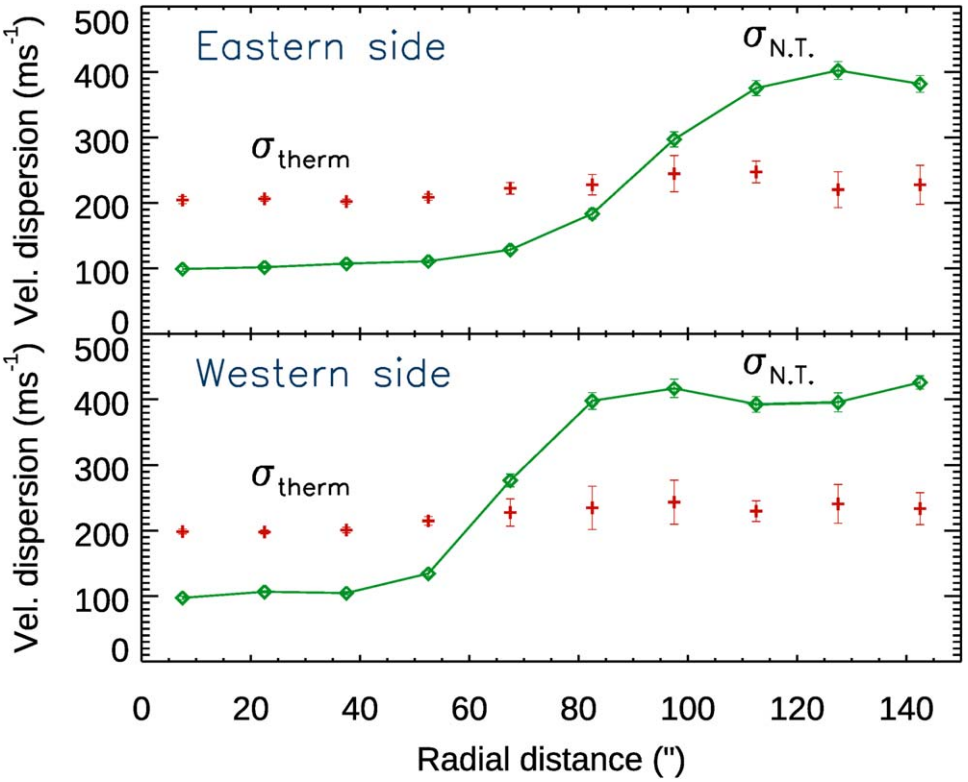

Figure C1. Thermal and nonthermal velocity dispersions as functions of the radial distance from the center on the eastern and western sides of H-MM1

ORCID iDs

Jorma Harju https://orcid.org/0000-0002-1189-9790
Jaime E. Pineda https://orcid.org/0000-0002-3972-1978
Anton I. Vasyunin https://orcid.org/0000-0003-1684-3355
Paola Caselli https://orcid.org/0000-0003-1481-7911
Stella S. R. Offner https://orcid.org/0000-0003-1252-9916
Alyssa A. Goodman https://orcid.org/0000-0003-1312-0477
Alexandre Faure https://orcid.org/0000-0001-7199-2535
Romane Le Gal https://orcid.org/0000-0003-1837-3772
Pierre Hily-Blant https://orcid.org/0000-0003-3488-8442
Luca Bizzocchi https://orcid.org/0000-0002-9953-8593
Andreas Burkert https://orcid.org/0000-0001-6879-9822
Hope Chen https://orcid.org/0000-0001-6222-1712
Rachel K. Friesen https://orcid.org/0000-0001-7594-8128
Philip C. Myers https://orcid.org/0000-0002-2885-1806
Anna Punanova https://orcid.org/0000-0001-6004-875X
Erik Rosolowsky https://orcid.org/0000-0002-5204-2259
Stephan Schlemmer https://orcid.org/0000-0002-1421-7281

References

Abid, M., & Verga, A. 2011, PhRvE, 84, 026318
Arzoumanian, D., André, P., Didelon, P., et al. 2011, A&A, 529, L6
Auddy, S., Myers, P. C., Basu, S., et al. 2019, ApJ, 872, 207
Bachiller, R., & Pérez Gutiérrez, M. 1997, ApJL, 487, L93
Bacmann, A., & Faure, A. 2016, A&A, 587, A130
Balucani, N., Ceccarelli, C., & Taquet, V. 2015, MNRAS, 449, L16
Batchelor, G. K. 1967, An Introduction to Fluid Dynamics (Cambridge: Cambridge Univ. Press)
Bertin, M., Romanzin, C., Doronin, M., et al. 2016, ApJL, 817, L12
Bizzocchi, L., Caselli, P., Spezzano, S., & Leonardo, E. 2014, A&A, 569, A27
Boogert, A. C. A., Gerakines, P. A., & Whittet, D. C. B. 2015, ARA&A, 53, 541
Bringa, E. M., & Johnson, R. E. 2004, ApJ, 603, 159
Burkert, A., & Bodenheimer, P. 2000, ApJ, 543, 822
Butler, M. J., & Tan, J. C. 2009, ApJ, 696, 484
Cardelli, J. A., Clayton, G. C., & Mathis, J. S. 1989, ApJ, 345, 245
Casassus, S., Dickinson, C., Cleary, K., et al. 2008, MNRAS, 391, 1075
Caselli, P., Hartquist, T. W., & Havnes, O. 1997, A&A, 322, 296
Caselli, P., Keto, E., Bergin, E. A., et al. 2012, ApJL, 759, L37
Caselli, P., Sipilä, O., & Harju, J. 2019, RSPTA, 377, 20180401
Cecchi-Pestellini, C., & Aiello, S. 1992, MNRAS, 258, 125
Chabot, M. 2016, A&A, 585, A15
Cheng, B.-M., Bahou, M., Chen, W.-C., et al. 2002, JChPh, 117, 1633
Chokshi, A., Tielens, A. G. G. M., & Hollenbach, D. 1993, ApJ, 407, 806
Cleeves, L. I., Bergin, E. A., & Adams, F. C. 2014, ApJ, 794, 123
Cleeves, L. I., Bergin, E. A., O'D. Alexander, C. M., et al. 2016, ApJ, 819, 13
Corcos, G. M., & Sherman, F. S. 1976, JFM, 73, 241
Cruz-Diaz, G. A., Martín-Doménech, R., Muñoz Caro, G. M., & Chen, Y.-J. 2016, A&A, 592, A68
Cuppen, H. M., van Dishoeck, E. F., Herbst, E., & Tielens, A. G. G. M. 2009, A&A, 508, 275
Damiani, F., Prisinzano, L., Pillitteri, I., Micela, G., & Sciortino, S. 2019, A&A, 623, A112
Daniel, F., Coudert, L. H., Punanova, A., et al. 2016, A&A, 586, L4
Dartois, E., Chabot, M., Id Barkach, T., et al. 2019, A&A, 627, A55
de Geus, E. J. 1992, A&A, 262, 258
d'Hendecourt, L. B., Allamandola, L. J., Baas, F., & Greenberg, J. M. 1982, A&A, 109, L12
Draine, B. T. 1985, in Protostars and Planets II, ed. D. C. Black & M. S. Matthews (Tucson, AZ: Univ. Arizona Press), 621
Dulieu, F., Congiu, E., Noble, J., et al. 2013, NatSR, 3, 1338
Faure, A., Hily-Blant, P., Rist, C., et al. 2019, MNRAS, 487, 3392
Flower, D. R., & Pineau des Forets, G. 1994, MNRAS, 268, 724
Friesen, R. K., Pineda, J. E., co-PIs, et al. 2017, ApJ, 843, 63
Fuente, A., Cernicharo, J., Roueff, E., et al. 2016, A&A, 593, A94
Gaches, B. A. L., & Offner, S. S. R. 2018, ApJ, 861, 87
Gaches, B. A. L., Offner, S. S. R., & Bisbas, T. G. 2019, ApJ, 878, 105
Garrod, R., Park, I. H., Caselli, P., & Herbst, E. 2006, FaDi, 133, 51
Garrod, R. T., & Herbst, E. 2006, A&A, 457, 927
Garrod, R. T., Wakelam, V., & Herbst, E. 2007, A&A, 467, 1103
Geppert, W. D., Hamberg, M., Thomas, R. D., et al. 2006, FaDi, 133, 177
Gilbert, A. D. 1988, JFM, 193, 475

Gong, H., & Ostriker, E. C. 2011, ApJ, 729, 120
Goodman, A. A., Barranco, J. A., Wilner, D. J., & Heyer, M. H. 1998, ApJ, 504, 223
Habing, H. J. 1968, BAN, 19, 421
Habing, H. J., & Israel, F. P. 1979, ARA&A, 17, 345
Harju, J., Daniel, F., Sipilä, O., et al. 2017, A&A, 600, A61
Hasegawa, T. I., & Herbst, E. 1993, MNRAS, 261, 83
Hily-Blant, P., Faure, A., Rist, C., Pineau des Forêts, G., & Flower, D. R. 2018, MNRAS, 477, 4454
Hily-Blant, P., Walmsley, M., Pineau Des Forêts, G., & Flower, D. 2010, A&A, 513, A41
Ho, P. T. P., & Townes, C. H. 1983, ARA&A, 21, 239
Hollenbach, D., Kaufman, M. J., Bergin, E. A., & Melnick, G. J. 2009, ApJ, 690, 1497
Ivlev, A. V., Padovani, M., Galli, D., & Caselli, P. 2015a, ApJ, 812, 135
Ivlev, A. V., Röcker, T. B., Vasyunin, A., & Caselli, P. 2015b, ApJ, 805, 59
Jiménez-Serra, I., Caselli, P., Martín-Pintado, J., & Hartquist, T. W. 2008, A&A, 482, 549
Jiménez-Serra, I., Vasyunin, A. I., Caselli, P., et al. 2016, ApJL, 830, L6
Johnstone, D., di Francesco, J., & Kirk, H. 2004, ApJL, 611, L45
Juvela, M. 2019, A&A, 622, A79
Kalvāns, J. 2018a, ApJS, 239, 6
Kalvāns, J. 2018b, MNRAS, 478, 2753
Kalvāns, J., & Kalnin, J. R. 2019, MNRAS, 486, 2050
Keto, E., Rawlings, J., & Caselli, P. 2014, MNRAS, 440, 2616
Kraichnan, R. H. 1967, PhFl, 10, 1417
Kraichnan, R. H. 1971, JFM, 47, 525
Laas, J. C., & Caselli, P. 2019, A&A, 624, A108
Larson, R. L., Evans, N. J., II, Green, J. D., & Yang, Y.-L. 2015, ApJ, 806, 70
Lazarian, A., & Yan, H. 2002, ApJL, 566, L105
Leger, A., Jura, M., & Omont, A. 1985, A&A, 144, 147
Liseau, R., White, G. J., Larsson, B., et al. 1999, A&A, 344, 342
Maret, S., Bergin, E. A., & Tafalla, M. 2013, A&A, 559, A53
Mathis, J. S., Mezger, P. G., & Panagia, N. 1983, A&A, 128, 212
Mathis, J. S., Rumpl, W., & Nordsieck, K. H. 1977, ApJ, 217, 425
Minissale, M., Dulieu, F., Cazaux, S., & Hocuk, S. 2016, A&A, 585, A24
Nummelin, A., Bergman, P., Hjalmarson, Å., et al. 2000, ApJS, 128, 213
Öberg, K. I., Garrod, R. T., van Dishoeck, E. F., & Linnartz, H. 2009, A&A, 504, 891
Ortiz-León, G. N., Loinard, L., Dzib, S. A., et al. 2018, ApJL, 869, L33
Ortiz-León, G. N., Loinard, L., Kounkel, M. A., et al. 2017, ApJ, 834, 141
Ossenkopf, V., & Henning, T. 1994, A&A, 291, 943
Oya, Y., Sakai, N., López-Sepulcre, A., et al. 2016, ApJ, 824, 88
Padovani, M., Galli, D., & Glassgold, A. E. 2009, A&A, 501, 619
Padovani, M., Marcowith, A., Hennebelle, P., & Ferrière, K. 2016, A&A, 590, A8
Parise, B., Belloche, A., Du, F., Güsten, R., & Menten, K. M. 2011, A&A, 526, A31
Patnaik, P. C., Sherman, F. S., & Corcos, G. M. 1976, JFM, 73, 215
Pattle, K., Ward-Thompson, D., Kirk, J. M., et al. 2015, MNRAS, 450, 1094
Perez-Becker, D., & Chiang, E. 2011, ApJ, 727, 2
Person, J. C., & Nicole, P. P. 1971, JChPh, 55, 3390
Pineau des Forêts, G., Roueff, E., Schilke, P., & Flower, D. R. 1993, MNRAS, 262, 915
Pineda, J. E., Goodman, A. A., Arce, H. G., et al. 2010, ApJL, 712, L116
Podio, L., Codella, C., Gueth, F., et al. 2015, A&A, 581, A85
Pon, A., Johnstone, D., Kaufman, M. J., Caselli, P., & Plume, R. 2014, MNRAS, 445, 1508
Pontoppidan, K. M. 2006, A&A, 453, L47
Preibisch, T., & Mamajek, E. 2008, in Handbook of Star-forming Regions, ed. B. Reipurth (San Francisco, CA: ASP), 235
Punanova, A., Caselli, P., Feng, S., et al. 2018, ApJ, 855, 112
Rawlings, M. G., Juvela, M., Lehtinen, K., Mattila, K., & Lemke, D. 2013, MNRAS, 428, 2617
Roberts, H., Herbst, E., & Millar, T. J. 2003, ApJL, 591, L41
Roberts, J. F., Rawlings, J. M. C., Viti, S., & Williams, D. A. 2007, MNRAS, 382, 733
Rodgers, S. D., & Charnley, S. B. 2001, ApJ, 553, 613
Shen, C. J., Greenberg, J. M., Schutte, W. A., & van Dishoeck, E. F. 2004, A&A, 415, 203
Shingledecker, C. N., Lamberts, T., Laas, J. C., et al. 2020, ApJ, 888, 52
Shulman, L. M. 2004, A&A, 416, 187
Sipilä, O., Caselli, P., Redaelli, E., Juvela, M., & Bizzocchi, L. 2019, MNRAS, 487, 1269
Sipilä, O., Harju, J., Caselli, P., & Schlemmer, S. 2015, A&A, 581, A122
Spezzano, S., Bizzocchi, L., Caselli, P., Harju, J., & Brünken, S. 2016, A&A, 592, L11
Spezzano, S., Caselli, P., Bizzocchi, L., Giuliano, B. M., & Lattanzi, V. 2017, A&A, 606, A82
Tafalla, M., Santiago-García, J., Myers, P. C., et al. 2006, A&A, 455, 577
Taquet, V., Charnley, S. B., & Sipilä, O. 2014, ApJ, 791, 1
Tielens, A. G. G. M., & Hagen, W. 1982, A&A, 114, 245
Vastel, C., Ceccarelli, C., Lefloch, B., & Bachiller, R. 2014, ApJL, 795, L2
Vasyunin, A. I., Caselli, P., Dulieu, F., & Jiménez-Serra, I. 2017, ApJ, 842, 33
Vasyunin, A. I., & Herbst, E. 2013, ApJ, 769, 34
Vidal, T. H. G., Loison, J.-C., Jaziri, A. Y., et al. 2017, MNRAS, 469, 435
Voelk, H. J., Morfill, G., Roeser, S., & Jones, F. C. 1978, M&P, 19, 221
Walmsley, C. M., Flower, D. R., & Pineau des Forêts, G. 2004, A&A, 418, 1035
Watanabe, N., & Kouchi, A. 2002, ApJL, 571, L173
Whittet, D. C. B., Gerakines, P. A., Hough, J. H., & Shenoy, S. S. 2001, ApJ, 547, 872
Yan, H., Lazarian, A., & Draine, B. T. 2004, ApJ, 616, 895